

# A Large Ungated TPC with GEM Amplification

M. Berger<sup>a,f</sup>, M. Ball<sup>a,b</sup>, L. Fabbietti<sup>a,f</sup>, B. Ketzer<sup>a,b,\*</sup>, R. Arora<sup>c</sup>, R. Beck<sup>b</sup>,  
 F. Böhmer<sup>a</sup>, J.-C. Chen<sup>a,f</sup>, F. Cusanno<sup>a,f,1</sup>, S. Dørheim<sup>a</sup>, J. Hehner<sup>c</sup>, N.  
 Herrmann<sup>e</sup>, C. Höppner<sup>a</sup>, D. Kaiser<sup>b</sup>, M. Kiš<sup>c</sup>, V. Kleipa<sup>c</sup>, I. Konorov<sup>a</sup>, J.  
 Kunkel<sup>c</sup>, N. Kurz<sup>c</sup>, Y. Leifels<sup>c</sup>, P. Müllner<sup>d</sup>, R. Münzer<sup>a,f</sup>, S. Neubert<sup>a</sup>, J.  
 Rauch<sup>a</sup>, C.J. Schmidt<sup>c</sup>, R. Schmitz<sup>b</sup>, D. Soyk<sup>c</sup>, M. Vandenbroucke<sup>a</sup>, B.  
 Voss<sup>c</sup>, D. Walther<sup>b</sup>, J. Zmeskal<sup>d</sup>

<sup>a</sup>*Technische Universität München, Physik Department, 85748 Garching, Germany*

<sup>b</sup>*Universität Bonn, Helmholtz-Institut für Strahlen- und Kernphysik, 53115 Bonn, Germany*

<sup>c</sup>*GSI Helmholtzzentrum für Schwerionenforschung GmbH, 64291 Darmstadt, Germany*

<sup>d</sup>*Stefan Meyer Institut für Subatomare Physik, Wien, Austria*

<sup>e</sup>*Universität Heidelberg, Heidelberg, Germany*

<sup>f</sup>*Excellence Cluster Origin and Structure of the Universe, 85748 Garching, Germany*

---

## Abstract

A Time Projection Chamber (TPC) is an ideal device for the detection of charged particle tracks in a large volume covering a solid angle of almost  $4\pi$ . The high density of hits on a given particle track facilitates the task of pattern recognition in a high-occupancy environment and in addition provides particle identification by measuring the specific energy loss for each track. For these reasons, TPCs with Multiwire Proportional Chamber (MWPC) amplification have been and are widely used in experiments recording heavy-ion collisions. A significant drawback, however, is the large dead time of the order of 1 ms per event generated by the use of a gating grid, which is mandatory to prevent ions created in the amplification region from drifting back into the drift volume, where they would severely distort the drift path of subsequent tracks. For experiments with higher event rates this concept of a conventional TPC operating with a triggered gating grid can therefore not be applied without a significant loss of data. A continuous readout of the signals is the more appropriate way of operation. This, however, constitutes a change of paradigm with considerable challenges to be met concerning the amplification region, the design and bandwidth of the readout electronics, and the data handling. A mandatory prerequisite for such an operation is a

sufficiently good suppression of the ion backflow from the avalanche region, which otherwise limits the tracking and particle identification capabilities of such a detector. Gas Electron Multipliers (GEM) are a promising candidate to combine excellent spatial resolution with an intrinsic suppression of ions. In this paper we describe the design, construction and the commissioning of a large TPC with GEM amplification and without gating grid (GEM-TPC). The design requirements have driven innovations in the construction of a light-weight field-cage, a supporting media flange, the GEM amplification and the readout system, which are presented in this paper. We further describe the support infrastructure such as gas, cooling and slow control. Finally, we report on the operation of the GEM-TPC in the FOPI experiment, and describe the calibration procedures which are applied to achieve the design performance of the device.

*Keywords:* Gas Electron Multiplier (GEM), Time Projection Chamber (TPC), Particle tracking, Particle identification, Ion backflow, FOPI, ALICE

---

## 1. Introduction

A gas-filled Time Projection Chamber (TPC) [1] with its low material budget, large solid-angle coverage and excellent pattern recognition capabilities is an ideal detector for three-dimensional tracking and identification of charged particles. TPCs have been already used in many experiments such as PEP-4 [2], ALEPH [3], DELPHI [4], NA49 [5, 6], and are currently being employed e.g. in STAR [7, 8] and ALICE [9]. In a conventional TPC, electron-ion pairs created by an ionizing particle within the drift volume are separated by an electric field. Electrons drift towards the readout anode, where they produce a charge avalanche in Multiwire Proportional Chambers (MWPCs) [10] which induces a detectable signal in the cathode pads. In order to prevent the ions produced in the avalanche from drifting back into the drift volume of the TPC, where they would severely distort the drift field, a switchable electrostatic gate must be employed. This, however, inevitably leads to dead times and limits the TPC readout rate to values of the order of few kHz.

---

\*Corresponding author

*Email address:* `Bernhard.Ketzer@cern.ch` (B. Ketzer)

<sup>1</sup>Deceased



In order to efficiently employ TPCs in experiments with high interaction rates, new techniques of ion-backflow suppression have to be found which do not require the use of a gating grid. Gas Electron Multiplier (GEM) foils [11] represent an optimal solution since they offer an intrinsic suppression of the ion backflow [12]. A GEM consists of a  $50\text{ }\mu\text{m}$  thin insulating polyimide foil with copper-coated surfaces, typically  $5\text{ }\mu\text{m}$  thick. The foil is perforated by photolithography and etching processes, forming a dense, regular hexagonal pattern of holes. In the standard geometry the holes have a double-conical shape with an inner diameter of  $\approx 50\text{ }\mu\text{m}$ , an outer diameter of  $\approx 70\text{ }\mu\text{m}$ , and a pitch of  $140\text{ }\mu\text{m}$ . Figure 1 shows an electron microscope image of a standard GEM foil. The small dimensions of the amplification structures lead

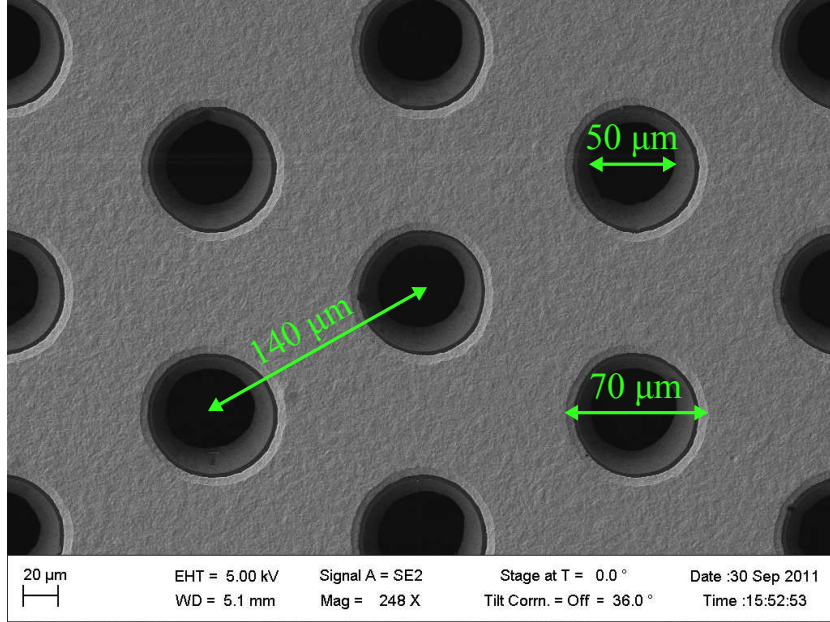


Figure 1: Electron microscope image of a GEM foil. The scale is given on the bottom left side.

to very large electric fields inside the holes of the GEM foil of the order of  $50\text{ kV cm}^{-1}$  if a moderate voltage difference of 200 V to 400 V (depending on the gas) is applied between the metal layers. Such fields are sufficient to create an avalanche inside the hole of the GEM foil. Avalanche electrons are extracted from the hole by the electric field applied below the GEM foil and can be further multiplied in subsequent GEM foils or collected at the anode.

Detectors based on a triple-GEM amplification have been pioneered by the COMPASS experiment at CERN [13, 14, 15, 16], and are now routinely used in several particle physics experiments like LHCb [17], PHENIX [18], and TOTEM [19]. New applications include the use of GEM-based detectors in KLOE-2 [20] and CMS [21].

Owing to their small diffusion, the ions created in the avalanche inside a GEM hole closely follow the electric field lines leading to the top side of the GEM foil and are collected there. Depending on the electric field settings, only a fraction of the ions created in the avalanche drifts back into the drift volume. This mechanism of ion backflow suppression is illustrated in Fig. 2.

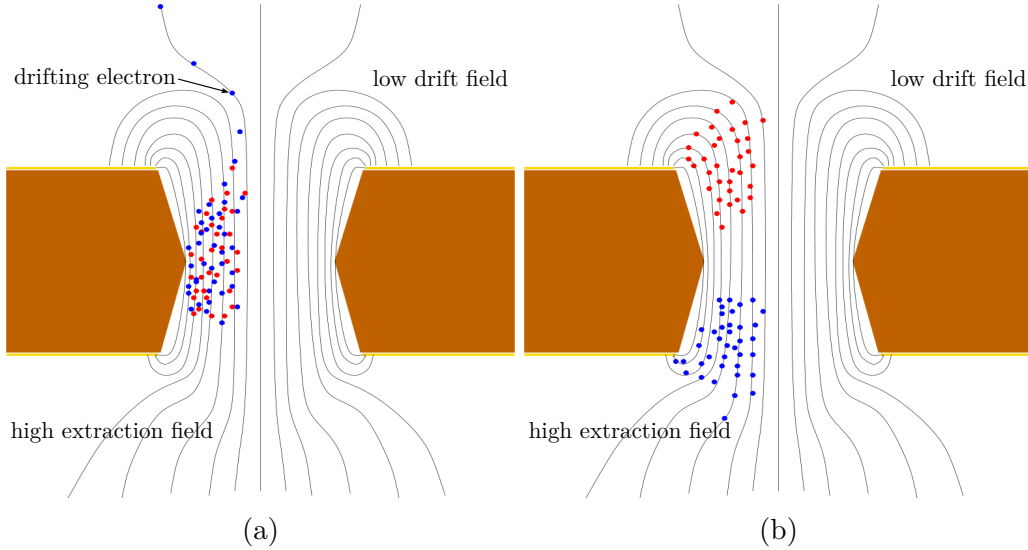


Figure 2: Suppression of ion backflow in a GEM: (a) electrons are guided into the holes by the low drift field, where avalanches of electron-ion pairs are generated. (b) The asymmetric field configuration of low drift field and higher extraction field together with the small ion mobility lead to efficient backflow suppression.

Although the ion suppression in a multi-GEM stack is of the order of  $10^{-2}$  to a few  $10^{-3}$  and hence does not reach the same level as a gating grid (see e.g. [22, 23] for a summary of the present status of ion backflow measurements), the resulting track distortions due to ion backflow are limited to a few cm, and can thus be corrected using advanced calibration techniques. This provides the possibility to operate a TPC without the gating grid in

a continuous, trigger-less mode, allowing an increase in event rate by two orders of magnitude, as foreseen e.g. in ALICE at CERN [24, 25].

In order to prove the concept of an ungated TPC with GEM amplification the detector presented in this paper was built. The GEM-TPC was commissioned with cosmic rays and with particle beams at the FOPI experiment at GSI in Darmstadt (Germany), and was employed for an experimental campaign with a secondary pion beam. This paper describes the design and construction of the GEM-TPC including the auxiliary systems which were custom-made for this detector. Section 2 gives a general overview of the design of the GEM-TPC. In section 3 the electro-mechanical design of the field-cage is presented, followed in section 4 by a detailed description of the so-called media flange, which hosts all supply connections and is the central support element of the detector. The GEM amplification stage is described in section 5, the pad-plane with hexagonal-shaped signal pads in section 6. The front-end electronics and the data acquisition system are discussed in section 7. Section 8 describes the cooling system for the front-end electronics, while the gas system and chosen gas mixture are presented in section 9. The slow control system used to operate the GEM-TPC detector is treated in section 10. Finally, in section 11 the results from the commissioning in the FOPI experiment are presented followed in section 12 by a discussion of the calibration procedures applied in order to reach the design performance of the GEM-TPC.

## 2. General Design

The GEM-TPC presented in this paper has a cylindrical shape with the two end-planes serving as cathode and anode, respectively, and an inner bore for the beam. The key parameters of the GEM-TPC are listed in Table 1.

The outer diameter of the TPC was chosen to fit inside the Central Drift Chamber (CDC) of FOPI (see section 11) while the inner diameter was chosen to host different target dimensions. The dimensions also match the requirements for the Crystal Barrel experiment at ELSA [26], so that a similar detector could be used as a tracking system in this experiment in the future. The design of the detector takes into account the fixed-target nature of the FOPI experiment, with the ionization electrons drifting in one direction only, different from the symmetric setup with a central cathode and two anodes as used in collider experiments. The cathode is oriented in the forward direction with respect to the beam, while the readout anode and the associated readout

Parameter	Value	Unit
Outer Dimensions:		
Inner Diameter	104	mm
Outer Diameter	309	mm
Total Length	843	mm
Active Volume:		
Inner Diameter	110.2	mm
Outer Diameter	299.0	mm
Drift Length	727.8	mm
Gas Volume	48	dm <sup>3</sup>
GEM amplification stage:		
Effective gain	$1 \cdot 10^3 - 2 \cdot 10^3$	
GEM thickness	50	μm
GEM pitch	140	μm
GEM hole Ø	70	μm
Transfer gaps	2	mm
Induction gap	4	mm
Electronics		
No. of readout pads	10,254	
ASIC	AFTER (T2K)	
Sampling clock	15.55	MHz
Buffer depth	511	samples
Dynamic range	120	fC
No. of front-end cards	42	
ADC resolution	11	bit
Sensitivity	393	$e^-/\text{ADC ch.}$
Average ENC	720	$e^-$

Table 1: Design parameters of the GEM-TPC.

electronics are situated in the backward region in order to minimize the material exposed to particles emitted in interactions with the target, which is mounted in the inner bore.

The detection gas is enclosed in a vessel formed by two concentric cylinders and the two end planes. In addition to containing the detector gas, this vessel also serves as field cage to realize the required uniform electric field parallel to the cylinder axis. In order to keep the multiple scattering and interactions of traversing particles as low as possible a very thin but rigid composite material is used for the field-cage. On the cathode side the field-cage vessel is closed by an end plate of similar sandwich structure as the field cage.

On the anode side a rigid flange called media flange is glued to the field-cage. The media flange is used to fix the detector to external structures and houses all the connections for gas supply, high voltage, low voltage and sensor read-out. Two further flanges are mounted to the upstream side of the media flange: the GEM flange housing the GEM stack, and the read-out flange holding the pad-plane, which is patterned with 10,254 hexagonal pads for a two-dimensional localization of the incoming charge. The printed circuit boards holding the front-end (FE) electronics are directly connected to the back side of the pad-plane in a fan-shaped arrangement and are supported by two rigid rings made of Aluminum. These flanges are fixed to the media flange by external metal clamp bands and are sealed by rubber O-rings. Figure 3 and Fig. 4 show a cross-section and a photo of the final large GEM-TPC, respectively.

The whole apparatus is therefore composed of three mechanically separable parts: the field-cage cylindrical vessel with the media flange, the GEM flange and the read-out flange. This modular setup allows an easy maintenance of the detector system and to supply and read out the GEM-TPC exclusively from the anode side. The GEM-TPC was mounted inside the existing FOPI spectrometer at GSI [27] and employed in experimental campaigns with hadron and secondary pion beams at intermediate energies of few GeV. One major innovation in this TPC is the construction of a light-weight field-cage (section 3) with a material budget below 1 % of a radiation length. This keeps the multiple scattering in front of the other sub-detectors small to prevent a deterioration of their tracking performance. The target position is chosen such that most of the produced particles are emitted in the forward direction, where the material budget of the TPC is lowest, while all the rigid support structures as well as the all infrastructure connections are located

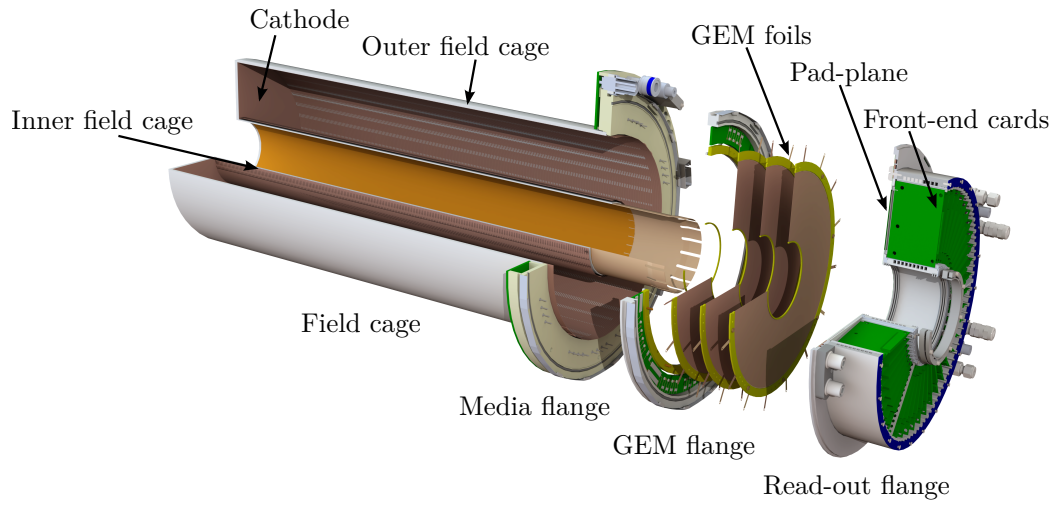


Figure 3: Cross-section of the large GEM-TPC.

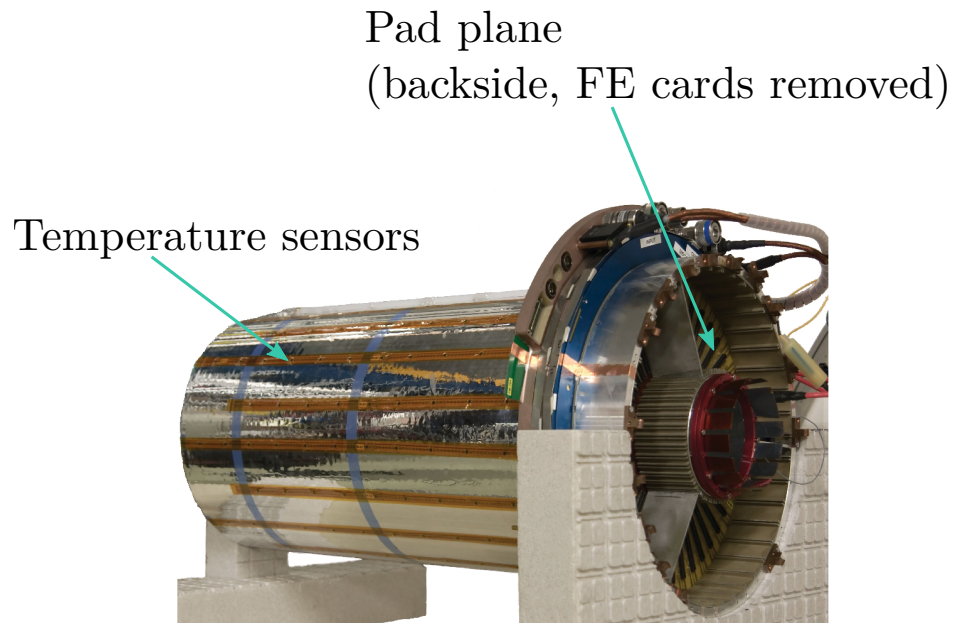


Figure 4: Photo of the large GEM-TPC.

upstream of the target position. Since the overall center of gravity of the TPC is close to the detector backward end-cap, only few fixation points at the media flange are necessary to hold the GEM-TPC in place. Another major achievement within this project is the adaption of the T2K AFTER chip (section 7) for the specific needs of the GEM-TPC.

### 3. Field-cage

#### 3.1. General Concept

Owing to physical and mechanical constraints, the cylindrical vessel of the TPC has to fulfill several requirements: it has to serve as gas container and field-cage at the same time, provide shielding of the HV to the outside while keeping the amount of material in forward and radial directions at the minimum. The main purpose of the integrated gas vessel and the field-cage is to define an electrostatic field with a relative homogeneity better than  $10^{-4}$  inside the gas volume to prevent that field inhomogeneities effect the detector resolution [9]. These requirements can be fulfilled employing a layered composite material. Because of its dual purpose realisation, the field-cage walls must be gas-tight and mechanically stable against changes in gas pressure and temperature. A temperature stability within  $1^\circ$  should be achieved during the system operation. The vessel should furthermore withstand a potential difference of about 30 kV between cathode and anode and must be electrically insulated.

#### 3.2. Technical Realisation

##### 3.2.1. Composite Material

The materials, the thicknesses of the different layers that compose the barrel walls and the cathode end-cap expressed in  $\mu\text{m}$  and in units of a radiation length are listed in the tables Table 2a and Table 2b, respectively. The layer stacking is sketched schematically in Fig. 5. One can see that the layout of the two concentric cylinders building the barrel walls and the cathode end-cap differ slightly. The cathode end-cap is composed of three Rohacell<sup>®</sup> layers to stabilize the structure and a further aluminized Kapton<sup>®</sup> foil is added to the side facing the gas volume to realize the cathode plane. The barrel and the cathode end-cap are joined together by gluing the extremities as shown in Fig. 6.

Special moulds were developed and constructed for the assembly of the

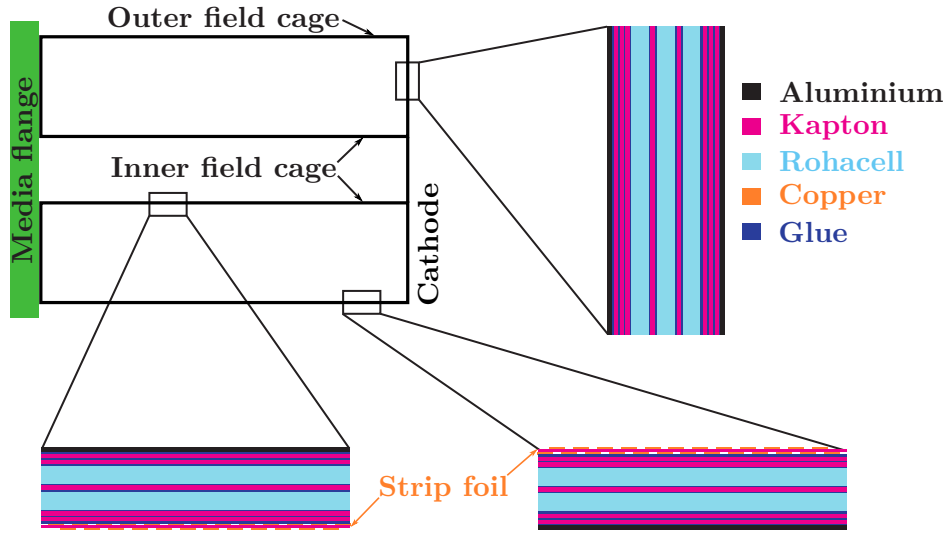


Figure 5: Cross-sections of the layout of the barrel and cathode end-cap walls, respectively. The shown layer stacking is not to scale.

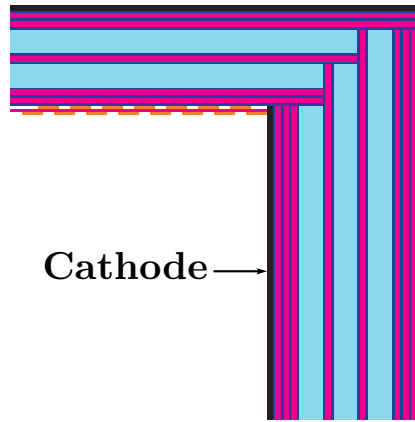


Figure 6: Cross-section of the interface between the field-cage barrel and the cathode end plane. The color code is the same as in Fig. 5.



Material	Thickness		Material	Thickness	
	( $\mu\text{m}$ )	(% $X_0$ )		( $\mu\text{m}$ )	(% $X_0$ )
Copper	5	0.035	Aluminium	0.2	0.0002
Kapton	25	0.009	Kapton	25	0.009
Copper	5	0.035	Kapton	25	0.009
Kapton	25	0.009	Kapton	125	0.045
Kapton	125	0.045	Rohacell	2000	0.026
Rohacell	2000	0.026	Kapton	125	0.045
Kapton	125	0.045	Rohacell	2000	0.026
Rohacell	2000	0.026	Kapton	125	0.045
Kapton	125	0.045	Rohacell	2000	0.026
Kapton	25	0.009	Kapton	125	0.045
Aluminium	0.2	0.0002	Kapton	25	0.009
Epoxy glue tot.	140	0.028	Kapton	25	0.009
Barrel Walls	4600	0.31	Aluminium	0.2	0.0002
			Epoxy glue tot.	140	0.028
			Cathode End-Cap	8900	0.33

Table 2: Materials, corresponding thickness of the layers that compose the barrel walls (a) and the cathode end-cap (b). The items are ordered from the inner to the outer surface of the field-cage.

cylindrical sandwich structures. The moulds are built by panelling an Aluminium cylinder with vacuum grooves with Metapor<sup>®</sup> slabs which are then milled into a cylindrical form. The outer strip foil or the inner strip foil are rolled around the respective mould and fixed by aspirating air through the porous Metapor material. The different materials are then glued successively on top of the previous layer. Vacuum bags are used to apply pressure and to flatten the layers during the gluing procedure of the sandwich structure. The vessel is electrically insulated by an additional Aluminium-coated Kapton layer of 30  $\mu\text{m}$  placed on its outside surface. This layer is connected to the detector-ground potential providing a shielded Faraday cage. Two gas supply lines and one HV line are attached to the outer field-cage parallel to the cylinder axis. The two gas lines are connected to the gas inlet realized with a Vespel<sup>®</sup> block hosting two inner channels. The block is inserted inside a cutout of the interface between the cathode and the field-cage to allow the gas flow through the channels into the cylinder. The high voltage supply cable is pierced through the field-cage and soldered onto a copper strip which in turn is glued with conductive adhesive onto the cathode.

The thickness of the field-cage vessel in units of a radiation length  $X_0$  was evaluated within the Root analysis framework [28]. A detailed geometry of the large GEM-TPC was created and the thickness was evaluated along tracks with different emission angles. The emission point for the considered particle tracks was placed on the central axis of the GEM-TPC at a distance of 30 cm upstream of the cathode plane (see Fig. 40). The obtained polar-angle dependence of the thickness in units of a radiation length  $X_0$  is shown in Fig. 7. At polar angles of  $\approx 9^\circ$  particles start to hit the inner field-cage wall in forward direction, causing a sharp increase of the material budget. Particles cross the cathode end plane of the field-cage up to an angle of  $\approx 26^\circ$ , traversing less material of the inner barrel wall with increasing polar angle. At  $\approx 26^\circ$  they start traversing both the inner and the outer barrel walls, which have a shorter radiation length than the cathode (see Table 2b), causing an increase in the material budget. The remaining smooth structure with a minimum at  $90^\circ$  reflects the thickness of the walls crossed by particles. Above a polar angle of  $160^\circ$  the thickness of the field-cage increases significantly (not shown in Figure 7) due to the large material budget of the media, GEM and readout flanges. For fixed target experiments such as FOPI where most of the tracks go in forward direction this high material budget in the backward direction has no impact on the overall detector performance.

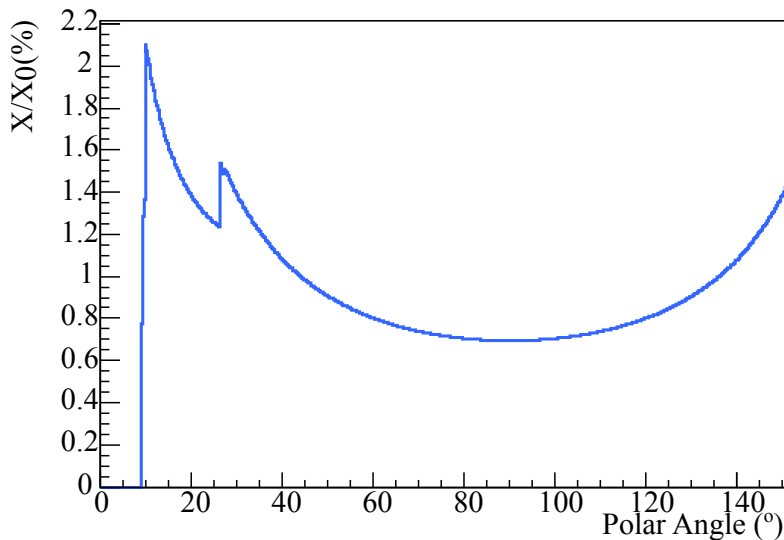


Figure 7: Total thickness of the field-cage vessel filled with Ar/CO<sub>2</sub> gas in units of a radiation length  $X_0$  plotted against the polar angle of particles emitted from the target position (see Fig. 40 for a sketch of the geometry).

### 3.2.2. Strip Foil and Voltage Divider

The layers of the inner and outer field-cage cylinders facing the gas volume are composed of 25  $\mu\text{m}$  thick foils of Kapton and FR4, respectively. Both foils are coated with copper on both sides.

Both copper surfaces are patterned in sets of parallel strips aligned transversally to the beam axis and staggered between the two sides in order to improve the homogeneity of the field. This way, 968 concentric cylindrical rings of copper with a width of 1 mm and a pitch of 1.5 mm cover the walls of the drift volume along the inner and outer radius, respectively. By connecting the strips with resistors a stepwise degrading potential is obtained, from the cathode value being about  $-30\text{ kV}$  to the potential of the last strip, close to the first GEM foil, with about  $-3\text{ kV}$ . Figure 8 shows a schematic view of the strip arrangement. The top view shown on the left panel of Fig. 8 indicates in red the outer strips which are facing outwards with respect to the gas volume and have special soldering pads to allow for the connection between neighbouring strips through resistors. The right panel of Fig. 8 shows schematic cross-sections of the strip foil. In Cut B the top of the Kapton foil with the two soldering pads of the neighbouring outer strips OS1 and OS2 are shown together with the contact pad placed between the two outer



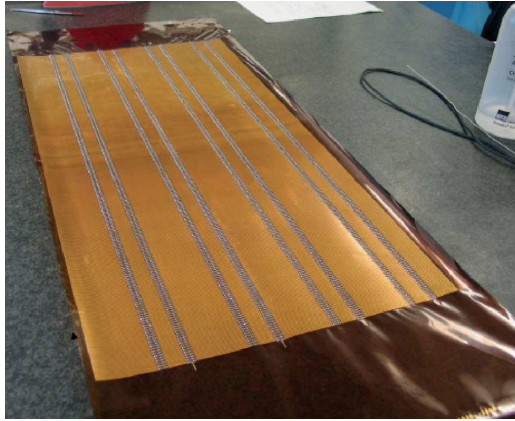


Figure 10: Photograph of the entire strip-line foil for the inner field-cage. The 8 rows with the SMD 0805 resistors that connect the strips are visible. See text for details.

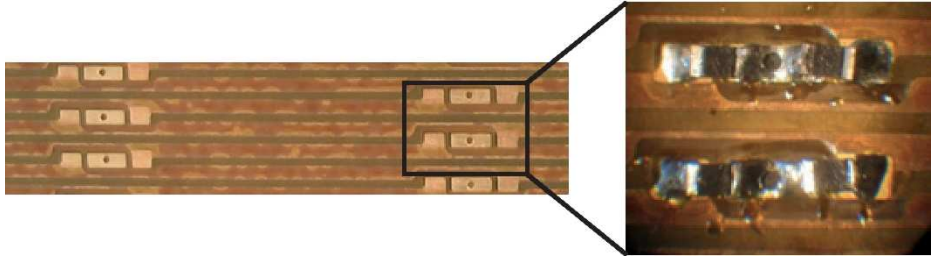


Figure 11: Photograph of the strip-line electrodes. The inset shows a photograph of the enlarged view on the SMD 0805 resistors soldered on the respective pads.

strips. The contact pad is directly connected to the inner strip IS2. The electric connection across the 25  $\mu\text{m}$  thick Kapton foil is represented by the green line and green circle in the right and left panel of Fig. 8, respectively. By placing the resistor  $R_1$  between OS1 and the contact pad one connects OS1 to IS2 and by placing a second resistor  $R_2$  one connects IS2 to OS2.

This way, all the 968 copper strips can be connected to build a resistor chain. Sequential connections are staggered to avoid contact between the resistors. Figure 9 shows the scheme of the resistor chain. Only half of the symmetric cross-section of the barrel is shown.  $U_{\text{Cathode}}$  and  $U_{\text{LS}}$  represent the cathode and the last strip potential, respectively. One can see that the end of the resistor chain is connected to a high voltage power supply. This allows not only to decouple the field-cage high voltage from the high voltage of the GEM amplification system but also to vary the potential of the last strip. This enables to adjust the electric field between the last strip and the first GEM foil in order to minimize the distortions at the junction between the field-cage and the first GEM foil.

Since the power supply used is not able to sink currents, a resistor  $R_{\text{GND}}$  of 20 M $\Omega$  connected to ground is placed between the power supply output and the last strip. This ensures a positive current output for the high voltage supply.

Each of the individual 4.2 M $\Omega$  0805 SMD resistors has a precision specification of 1 %. The resistors were measured by hand and four elements were grouped in parallel such that the precision of the total resistance per step could be increased to the needed value of 0.1 %. The total resistance between two adjacent strips is then 1.05 M $\Omega$ . This results in a total resistance  $R_{\text{F}}$  of 1014.3 M $\Omega$  over the resistor chain for the inner and outer cylinder, respectively.

Figure 10 shows a photograph of the entire strip-foil of the inner field-cage. One can see the 8 rows of resistors resulting from the parallel connection and the staggering connecting the inner to the outer strips. Figure 11 shows an enlarged version of the previous image where the outer strips and the soldered resistors are visible. Due to the limitation of the maximal width of the FR4 base material to 600 mm, the outer strip-foil is assembled by splicing two FR4 foils together where the splicing runs in parallel to the strips of the field-cage. Since the two spliced foils have to be electrically connected a copper bridge is soldered in between these two foils. This interconnection can be seen in Figure 12. A finite-element simulation of the GEM-TPC field-cage was carried out to investigate the homogeneity of the drift field. A two



Figure 12: Copper bridge soldered onto the field-cage strips at the border of the two spliced strip-foils.

dimensional geometry has been used exploiting the rotational symmetry of the GEM-TPC and different settings of the potentials have been considered to emulate the ideal and the real setup. The resulting field distortions within the drift volume were evaluated.

Figures 13-16 show the simulated two-dimensional maps of the electric field for the ideal and real setups, respectively. The color code shows the values of the radial and the longitudinal electric field components, respectively, for the different settings. The ideal set-up corresponds to the mechanical specifications given so far and to the following voltage settings for the cathode, last strip and top side of the first GEM foil:  $U_{\text{CATHODE}} = -25\,802.4\text{ V}$ ,  $U_{\text{LS}} = -3612.6\text{ V}$  and  $U_{\text{GEM1}} = -3458.6\text{ V}$ . These settings lead to a longitudinal electric field of  $309.6\text{ V cm}^{-1}$  in the center of the drift volume. Figure 13 shows the radial and longitudinal components of the electric field close to the cathode for the ideal case; the left panel shows also a schematic representation of the first three strips close to the cathode. Figure 14 shows the two field components close to the last strip for the ideal settings. Despite these expected local variations of the field close to the field-defining structures, the required field homogeneity of  $10^{-4}$  is reached at a maximal distance of  $2.2\text{ mm}$  from the field cage walls, corresponding to  $95.6\%$  of the total gas volume, provided that the mechanical specifications are met.

The connection of the first strip to the cathode is realised via conductive glue; during the construction of the field-cage, however, the first three strips

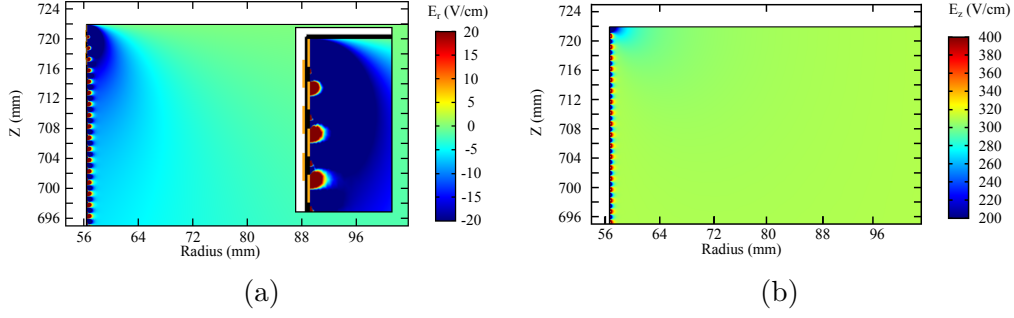


Figure 13: Results of a finite-element simulation of the 2-D map of the electric field in the radial (left panel) and  $z$  (right panel) direction in the region close to the cathode for an ideal set-up. See text for details.

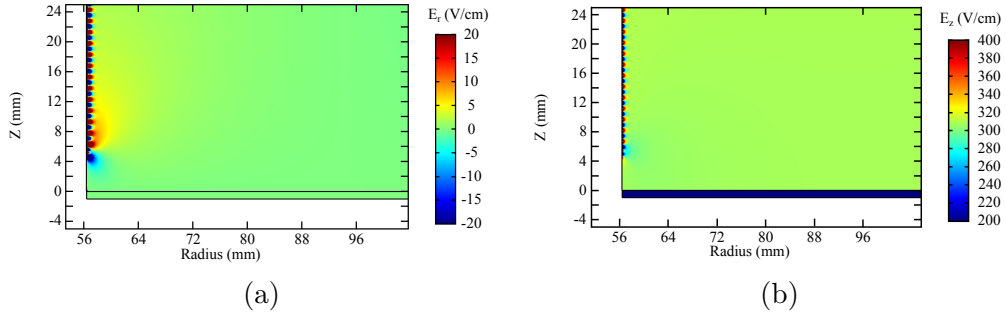


Figure 14: Results of a finite-element simulation of the 2-D map of the electric field in the radial (left panel) and  $z$  (right panel) direction in the region close to the last strip for an ideal set-up. See text for details.



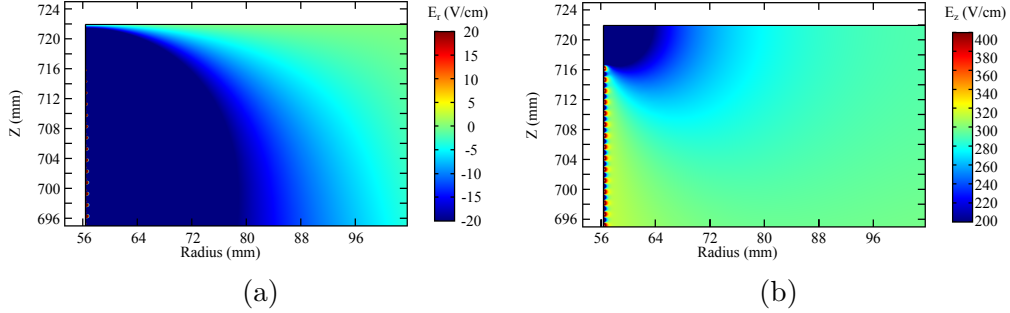


Figure 15: Results of a finite-element simulation of the 2-D map of the electric field in the radial (left panel) and  $z$  (right panel) direction in the region close to the cathode for the real set-up. See text for details.

on the outer and the first four strips on the inner cage were short-circuited by accident and are therefore at the same potential as the cathode. This configuration modifies the field close to the cathode surface as shown in Fig. 15, where the same quantities as in Fig. 13 are presented for the real setup. Moreover, during the detector commissioning too low a voltage was set to the last strip:  $U_{\text{CATHODE}} = -25\,940\text{ V}$ ,  $U_{\text{LS}} = -3528.6\text{ V}$  and  $U_{\text{GEM1}} = -3458.6\text{ V}$ . These settings lead to a longitudinal electric field of  $309.9\text{ V cm}^{-1}$  in the center of the drift volume, which is very similar to the ideal setting, but also to an additional radial component of the electric field close to the last strip and the first GEM foil as one can see in Fig. 16. The copper bridge used to connect the two spliced foils of the outer strip foil introduces further field distortions as shown in Figure 17. There panels a) and b) show the introduced distortions in the radial component and along the  $z$ -direction of the electric field, respectively. These distortions are calculated with the ideal setting mentioned above. The resulting distortions at the copper bridge for the real setting are not shown as they do not differ from the ideal setting. The deviation of the drift field obtained for the real setup are summarized in Fig. 18. Panel a) of Fig. 18 shows the deviation from zero of the radial component of the electric field as a function of the radius and the  $z$  position and panel b) presents the deviation of the  $z$ -component of the electric field from the nominal value as a function of the same spatial coordinates.

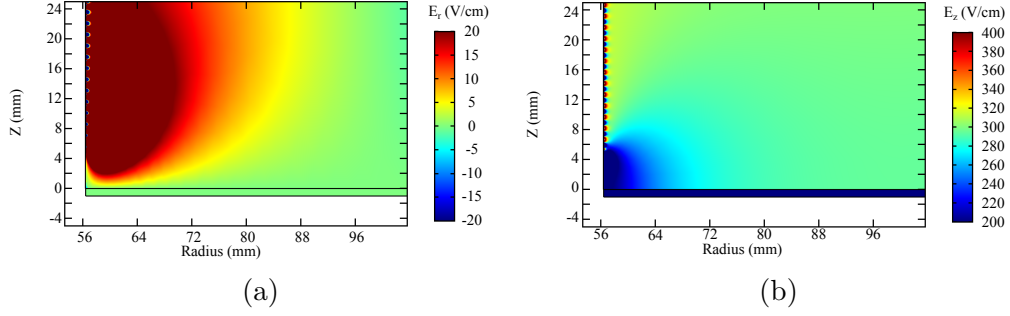


Figure 16: Results of a finite-element simulation of the 2-D map of the electric field in the radial (left panel) and  $z$  (right panel) direction in the region close to the last strip for the real set-up. See text for details.

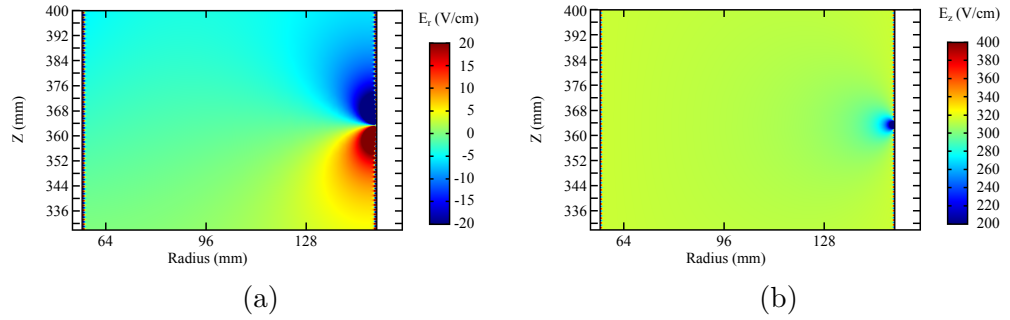
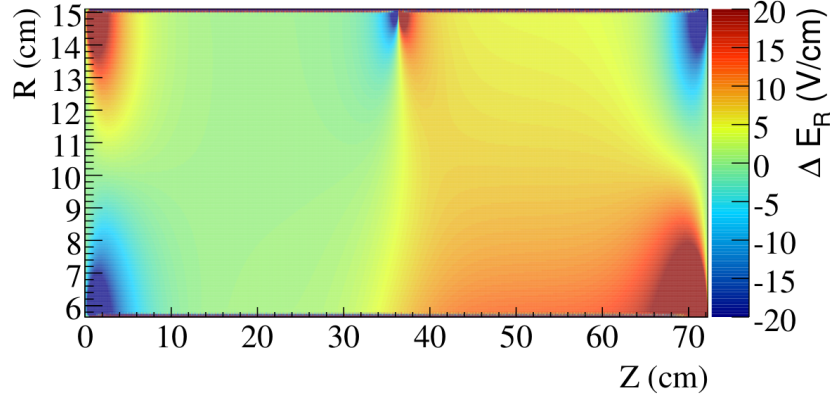
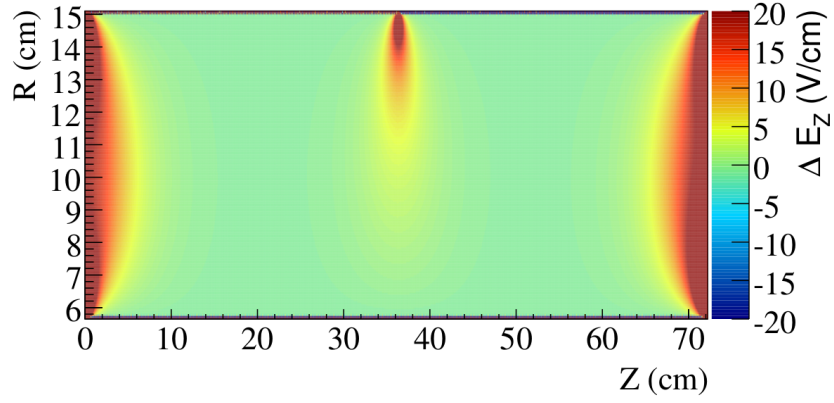


Figure 17: Results of a finite-element simulation of the 2-D map of electric field in the radial (left panel) and  $z$  (right panel) direction in the region close to the strip foil splicing for the ideal set-up. See text for details.



(a)



(b)

Figure 18: Deviation from the nominal field in radial (a) and longitudinal (b) direction as a function of the radius and  $z$  position. The nominal radial field is  $0 \text{ V cm}^{-1}$ , the nominal longitudinal field is  $309.6 \text{ V cm}^{-1}$ .

#### 4. Media Flange

The media flange is a rigid support flange which is glued to the field-cage vessel. It provides mechanical stability and serves as a mounting structure for the whole detector, is the main support for the GEM and readout flanges and provides the interfaces for all external supplies like gas, high voltage and sensors for measuring gas flow, temperature and pressure. Figure 19 displays a photo of the media flange glued onto the field-cage vessel. It is made of

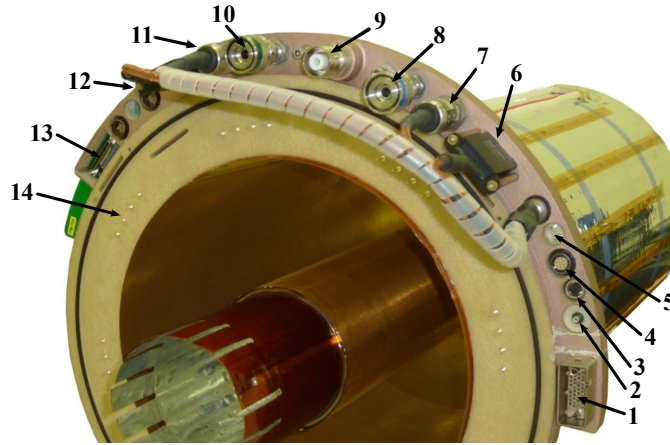


Figure 19: Photograph of the media flange glued to the field-cage, with (1) high-voltage connection for GEM foils, (2) pin for last strip high voltage, (3) connector for field-cage temperature sensors, (4) connector for gas flow and pressure sensors, (5) pins for ground connection, (6,12) mass flow meters, (7,11) pressure sensors, (8) gas outlet, (9) cathode high-voltage connection, (10) gas inlet, (13) connector for pad-plane temperature sensors, (14) pins for GEM-foil high voltage.

two pieces glued together in order to create internal channels which are used for the distribution of the gas. The main material used in the fabrication of the media flange is Stesalit 1011. The gas in- and outlets are realized by quick coupling connectors, type Swagelok Instrumentation Quick-Connect QC4. The high voltage for the drift cathode is supplied via a Radiall socket, type R341018. The high voltages for the GEM electrodes (6 channels) and the last strip of the field-cage are supplied via a multi-pin REDEL socket, type SLG.H51. The GEM high voltage channels are distributed through the media flange via pins to the GEM flange (see section 5). The last strip channel is connected within the media flange to the outer field-cage and via

an external cable to the inner field-cage. An additional cable connects the inner field-cage via the resistor ( $R_{\text{GND}}$  in Fig. 9) to ground.

To measure the pressure at the gas inlet and outlet, two compact pressure transducers, type Measurement Specialties M5141, are mounted on the media flange. They are suited for measuring the pressure in the range from 0 bar to 3.5 bar. Additionally, there are two Sensirion ASF 1400 mass flow meters, installed in series with the inlet and outlet gas channel. All sensor signals are read out by the GEM-TPC Slow Control system, described in section 10. In order to fix the inner field-cage to the readout flange, it ends on the anode side with Kapton flaps that are used to connect it to a two-piece support ring. Figure 20 shows how the flaps are inserted into the slotted holes of the upper support ring. The two parts of the support ring are screwed together clamping the flaps in between them. Finally, the whole structure is screwed to the mounting system for the FE cards. By adjusting the longitudinal position of the ring the tension and therefore the rigidity of the inner field-cage can be controlled.

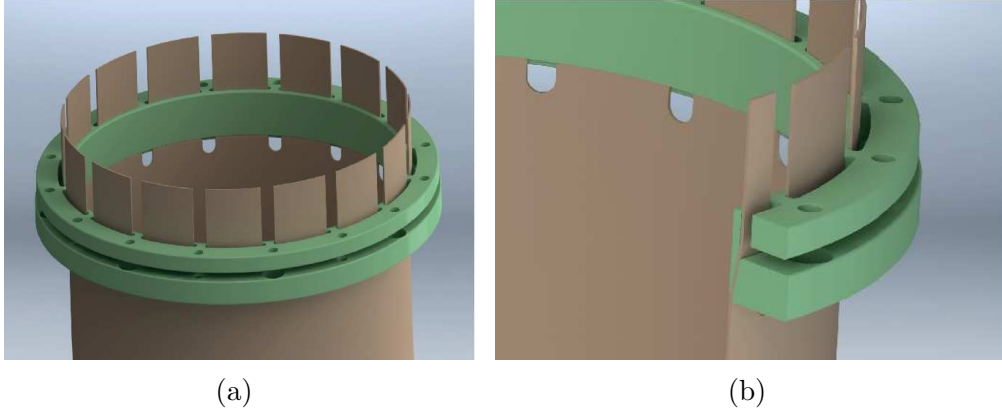


Figure 20: (a) Schematic view of the support ring used to fix the inner field-cage flaps to the flange. (b) Details of how the flaps are inserted in the slotted holes of the support ring.

## 5. The GEM Amplification Stage

### 5.1. GEM Design, Framing and Implementation

The GEMs are designed to fit to the dimensions of the GEM-TPC, so that the inner and outer radii of the GEM active area match the inner and outer



Figure 21: (a) Photograph of a framed GEM in the GEM flange. The green contour shows one of the eight sectors. (b) HV flap that connects the GEM foil to the HV distribution board (red PCB in the figure).

radius of the TPC field cage, respectively. This results in an active area of the GEM foil of around  $630\text{ cm}^2$ . One side of each GEM foil is divided into eight sectors to decrease the capacitance of each sector reducing significantly the discharge probability as well as the amount of stored charge which has to be dissipated in the case of a discharge [29]. This segmentation furthermore allows an operation of the TPC even in case of several non-operational sectors per foil. The eight sectors are shaped like aperture blades (see Fig. 21 a) and are separated by  $400\text{ }\mu\text{m}$  thick insulating borders where the copper layer was etched away. Each sector has a flap on the outer radius to connect it to the high voltage distribution board located inside the GEM flange (see Fig. 21 b). The high voltage distribution board also contains  $10\text{ M}\Omega$  bias resistors for each sector. As the distance between two GEM foils or a GEM foil and the read-out anode determines the field strength, a well defined and constant spacing throughout the whole foil has to be maintained. This is achieved by gluing  $1\text{ mm}$  thick FR4 frames onto each side of a foil while applying tension to the foil. The frames and their dimensions are depicted in Fig. 22.

The foil is stretched by applying tension on the four sides of the uncut rectangular foil. To this end, the foil edges are clamped between two fixation blocks where the lower one is movable and has a silicone rubber inlay to provide the necessary friction. The upper block fixes the edge to the lower block. By moving the fixation blocks with the help of screws, the foil can be

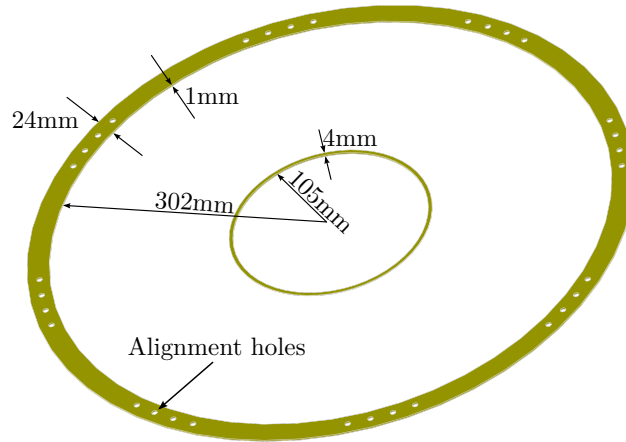


Figure 22: The inner and outer frame for the GEM foils with their dimensions and the alignment holes for installation inside the GEM flange.

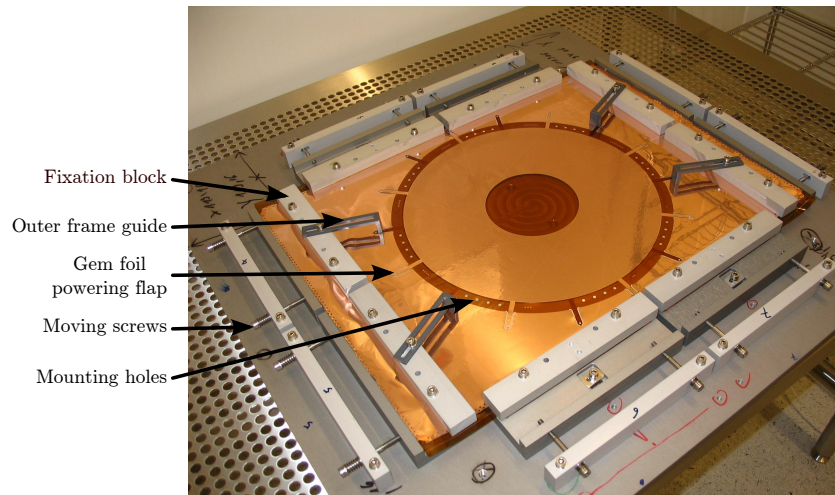


Figure 23: A GEM foil clamped inside the stretching tool during framing. One of the eight sectors is marked by a green line.

stretched until no wrinkles are left. Figure 23 shows an uncut foil mounted inside the stretching tool and stretched via the fixation blocks.

When the GEM foil is completely flat the inner and outer FR4 rings are glued on the upper side of the GEM foil with Araldite AW106 (hardener: 953U). Alignment holes are distributed along the outer circumference of the GEM foil and on the outer FR4 frame. The alignment holes on the outer GEM frame are visible in Fig. 22. The outer ring is aligned by placing pins through the alignment holes of the frames and the GEM foils into holes on the metal plate underneath the foil. A special tool employing the same alignment pins as for the outer ring is used for the deployment of the inner ring. This tool is basically a metal plate with concentric groves for the two frames which holds the inner frame with the help of a small air pump. This metal plate additionally serves as a weight to apply pressure on both rings while curing the glue. The glue is cured for about ten hours at a temperature of around 60°.

In the next step the foil is flipped and the whole procedure is repeated for the other side of the GEM foil. After the stretching and framing procedure is completed the unnecessary material around the outer frame is removed. The framed GEM foils are then permanently under tension and flat and can be assembled into a stack fixed to the GEM flange. Before, during and after the gluing high voltage tests of the GEM foils are performed to ensure the functionality and high voltage stability. To perform these tests, the foil is set under nitrogen atmosphere and voltages up to 550 V are applied to each sector via a 10 M $\Omega$  bias resistor, while all remaining sectors as well as the un-segmented side are grounded. The ramping scheme and the dwell time for each HV step are listed in Table 3. In Fig. 21 one can see a framed GEM mounted in the GEM flange.

The GEM flange can hold up to four GEM foils which are rotated with respect to each other to allow for a proper mounting of the flaps to the HV distribution. The positioning of the framed GEM foils is realized with alignment pins. Finally, the flaps of each sector are connected to their corresponding high voltage pin on the distribution board, visible in red in Fig. 21, which is also mounted inside the GEM flange. The unsegmented side of a GEM foil is connected with just one flap to the high voltage distribution board. Pins connect the high voltage distribution board to the media flange where a Redel connector (Fig. 19(1)) is placed to connect the GEM-TPC to the high voltage module. The frames with their thickness of 1 mm define the spacing in-between two GEM foils as shown in Fig. 24.



Voltage (V)	Dwell time
100	Until currents are stable
300	Until currents are stable
400	Until currents are stable
450	1 min
500	3 min
550	3 min
0	Until currents are stable
550	3 min

Table 3: High voltage test ramping scheme.

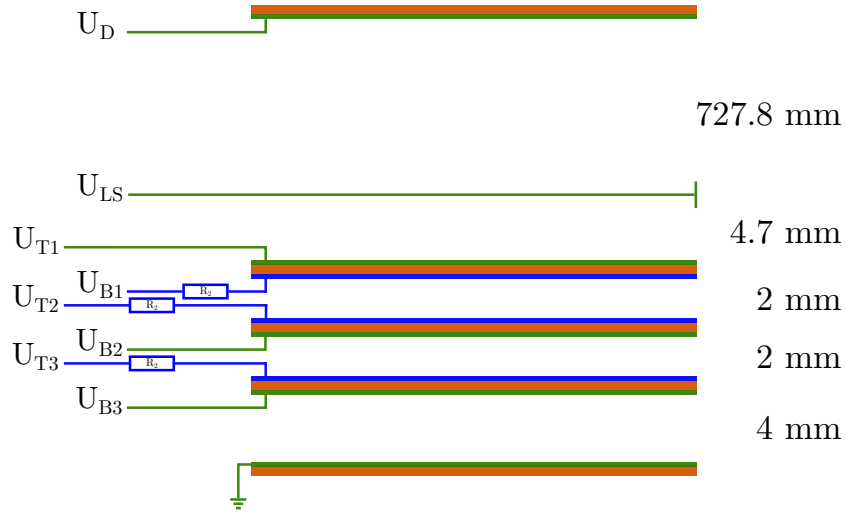


Figure 24: Nominal HV scheme of the GEM-TPC where  $U_D$  is the drift voltage,  $U_{LS}$  is the voltage of the last strip before the GEM foils and  $U_{Ti}$  and  $U_{Bi}$  are the top and bottom voltages of GEM foil  $i$ , respectively. The segmented sides of the foils are depicted in blue, the unsegmented in green. The spacings between the foils are indicated as well.

### 5.2. GEM HV scheme

For the sake of flexibility, we chose an HV supply for the GEM stack which includes a separate HV channel for each side of a GEM foil. On the one hand, operation with a resistor chain is known to be more reliable and stable because it avoids by design that large potential differences build up between electrodes in case of a trip of a single sector or in case of different time constants of discharging the foils. On the other hand, it is not possible in this configuration to test different voltage settings, which was an important asset for the present detector.

In the nominal configuration, the three GEM foils in a stack are mounted with the sectorized side facing the drift region [13]. Each sector is powered through a separate bias resistor ( $R_2=10\text{ M}\Omega$ , Fig. 25) in order to limit the current in case of a discharge. The upper limit of  $R_2$  is determined by the fact that the voltage drop across the GEM due to charge produced in the detector should remain small, such that the gain is not affected by the particle rate. The unsectorized side of a foil does not have a bias resistor, but is connected directly to the power supply. This configuration has the virtue of fixing the potential at the bottom side of each GEM to its nominal value in case of a discharge, thus avoiding excessive potential differences to the next stage or to the readout anode and effectively preventing discharges from propagating to the next stage. In addition, such a scheme allows for an operation of the detector even in case of permanent short circuits in several sectors. For a TPC, however, such a scheme is not directly applicable, because, at least for the top GEM directly facing the drift volume, the homogeneity of the drift field would be severely distorted by one sector at a potential which is different from the others. Therefore, at least the top GEM has to be mounted with the sectorized side facing the anode. The other foils should be mounted in the standard orientation, as shown in Fig. 24.

Due to an error in the design, however, a flipping of the GEM foils is not possible for the detector described in this paper. Therefore, all foils have to be mounted with the sectorized side facing the anode. To limit the increase of the potential on the lower side of the GEM in case of a discharge, a  $10\text{ M}\Omega$  bias resistor is mounted also for the unsectorized side ( $R_1$ ). The resulting configuration, which is shown schematically in Fig. 25, puts additional constraints onto the operational scheme, which has to be coped with during the operation: (i)  $V_{\text{top}}$  needs to be increased when a short circuit appears (switches in Fig. 25) because of the additional voltage drop over  $R_1$ , which limits the numbers of bad sectors due to the voltage limit of the power sup-

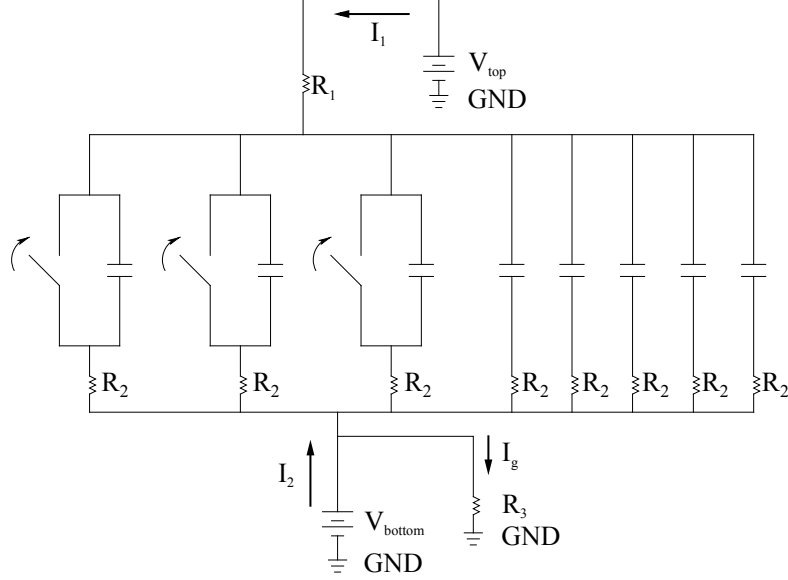


Figure 25: An equivalent circuit for a GEM foil. The switches illustrate the possibility of a shortcut sector due to a discharge.

ply. (ii) In case of a high particle rate, the resulting current produced in the detector leads to a larger voltage drop over  $R_1$  and  $R_2$  than for the nominal configuration with only  $R_2$ . Each GEM foil is powered by two independent channels of an ISEG EHS 8060n high voltage module. In case of a shortcut sector the voltage drop over the grounding resistor  $R_3$  prevents currents from flowing into the high voltage supply.

In conclusion, the adopted power supply scheme, although flexible, turned out to be not the optimal choice, and for stable operation at fixed settings should be replaced by a simple voltage divider (possibly exchangeable if flexibility is needed), or a stack of floating power supplies.

## 6. The Pad-Plane

The charge cloud emerging from the last GEM induces a negative, fast electron signal on the readout pads. For single incoming electrons, the FWHM of the induced signal is of the order of  $400\text{ }\mu\text{m}$ , depending on the transverse diffusion between the GEM stages and the spread inside the GEM holes. Consequently, a pitch of the readout elements of the same order of magnitude would be required to profit from a center-of-gravity reconstruction. For

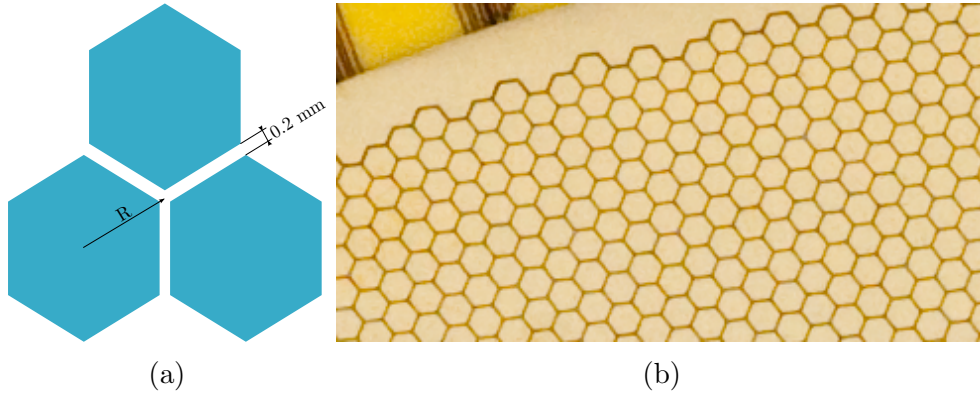


Figure 26: (a) Geometry of the pads indicating the radius and the distance between two pads. (b) Closeup view of the pad-plane.

a TPC, however, transverse diffusion of the ionization electrons during their drift to the amplification stage will dominate the precision with which its original position can be reconstructed, except for very small drift distances. The pad size should then be chosen such that the transverse diffusion for a given gas mixture and magnetic field dominates the resolution, and not the pad size. Furthermore the geometrical configuration of the pads should prevent a deterioration of the spatial resolution of the tracks due to angular effects. The pad-plane used for this GEM-TPC is designed following these guiding principles.

For a uniform charge distribution independent of the crossing angle of tracks, pads with a hexagonal shape are chosen. The optimum outer pad radius ( $R$ ) was determined to be 1.5 mm with the help of Monte Carlo simulations assuming a Ne/CO<sub>2</sub> (90/10) gas mixture and a magnetic field of 2 T, as originally foreseen for the TPC of the PANDA experiment. The definition of the pad radius is depicted in Figure 26 in the left panel. The gaps between the pads are 200  $\mu\text{m}$  wide. As one can see in Figure 27 these simulations show that the spatial resolution and hence the momentum resolution does not improve for outer radii of the hexagonal pads below 1.5 mm, as diffusion in the drift volume is the dominant contribution to the localization accuracy.

The pad-plane is realized as a printed circuit board (PCB) made of FR4 with 35  $\mu\text{m}$  thick gold-plated Cu pads. Figure 26 (b) shows a photographic image of the pad-plane, which in total has 10,254 readout pads. Since the

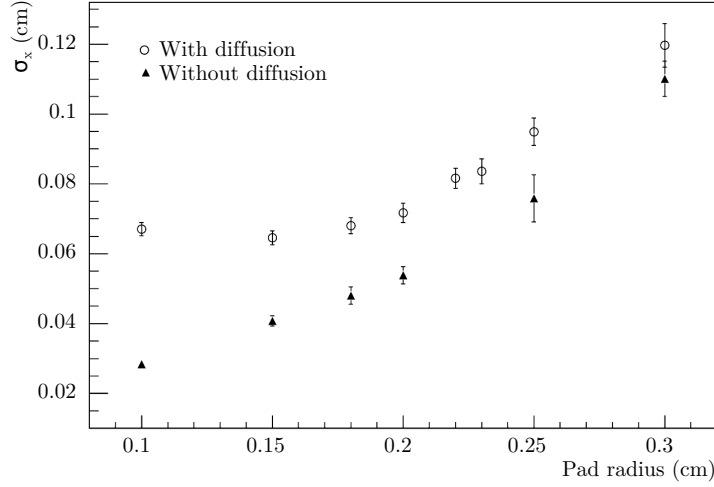


Figure 27: Standard deviation of residuals plotted against the pad radius with diffusion (circles) and without (triangles). A magnetic field of 2 T was applied to the simulation.

pad-plane is also used to close the gas volume it had to be designed in a gas-tight way. This is done by using a four-layer PCB with signal tracks on all layers and staggered connections between neighboring layers. On the backside of the pad-plane the signal lines are routed to 42 high-density connectors (Samtec BTH-150-01-F-D-A) with 300 pins and a pitch of 0.5 mm each. The connectors are arranged radially.

To avoid crosstalk between different pads the connections from the pads to the connectors are designed to minimize crossing of tracks or narrow parallel tracks of neighboring pads. Field inhomogeneities on the outer part of the pad-plane are avoided by placing copper areas, matching the shape of the pads, as shown in Fig. 26 (b). Further details about the construction of the pad-plane can be found in [30].

## 7. Front-end Electronics and Data Acquisition

### 7.1. General Requirements

The current signal seen by the charge-sensitive amplifier (CSA) connected to a readout pad is determined by the convolution of two distributions. The first is the ionization-charge distribution along the drift direction at the moment when it reaches the GEM foils. The spread of the charge is caused by the longitudinal diffusion of electrons during their drift through the TPC gas

volume. The second is the shape of the current pulse induced by electrons drifting from the last GEM electrode to the readout pad, which has a negative polarity with a fast risetime and a duration of about 50 ns. The length of the convoluted signal depends on the drift length. For the GEM-TPC considered here it is about 100 ns on average. The CSA is followed by a shaper with a programmable peaking time between 100 and 200 ns for optimization of the signal-to-noise ratio and the effect of pile-up. The sampling rate has to be adapted to the shaper output and should thus be chosen between 10 and 20 MHz. A crucial parameter for a continuously operating TPC is the noise level of the readout system, which has to be as low as possible ( $< 1000 e^-$ ) in order to operate the chamber at the minimum possible gain, defined by the required signal-to-noise ratio. A low gain in turn minimizes the ion backflow and the resulting track distortions. To allow for a continuous readout of the TPC, the front-end chip has to be able to simultaneously sample the incoming data and transfer the processed data to the next stage. Power consumption should be minimized to a level of  $\sim 20 \text{ mW/channel}$  to avoid the necessity of excessive cooling of the front-end cards. Last but not least, the chip has to be highly integrated to match the channel density on the pad plane.

The SAMPA chip [31] which is currently being developed for the upgrade of the ALICE TPC will fulfill all of the above requirements. At the time of the design and construction of the GEM-TPC no chip that matched all these requirements was available. The AFTER T2K chip [32] was chosen as a good compromise because it fulfils the low noise, low power consumption and high integration requirements. It does not allow, however, on-chip zero suppression and to concurrently sample and transfer the data.

## 7.2. The AFTER ASIC

The AFTER chip is a low-noise, low-consumption analog pipeline ASIC developed for the T2K near detector TPCs and fabricated in  $0.35 \mu\text{m}$  CMOS technology [33]. It has 76 channels, of which 72 are connected to input pins, each with a tunable preamplifier/shaper followed by a 511-cell switched capacitor array (SCA) analog memory. In Fig. 28 a simplified functional diagram of a single channel of the AFTER ASIC is shown. The main parameters of the AFTER ASIC can be found in Table 4. The preamplifier charge range can be chosen to be from 120 fC to 600 fC. The shaper has an adjustable peaking time in the range from 116 ns to 1.9  $\mu\text{s}$ . After the shaper the signals are sampled into an analog buffer which is implemented as two SCAs, each

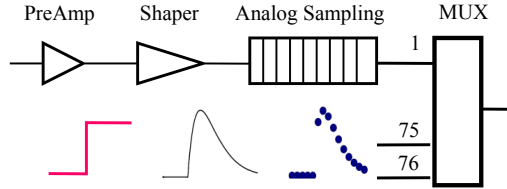


Figure 28: AFTER data flow.

Parameter	Value
Number of input channels	72
Samples per channel	511
Noise (nominal)	500 e <sup>-</sup> at 10 pF
Dynamic range	120 to 600 fC (4 values)
Peaking time	116 ns to 1.9 $\mu$ s (16 values)
Sampling frequency	1 to 50 MHz
Readout frequency	20 MHz
Power Consumption	6.2 to 7.5 mW/Channel
Size of the package	7.8 $\times$ 7.4 mm <sup>2</sup>

Table 4: Main parameters of the AFTER ASIC [33]

with 36 channels, and a depth of 511 samples. Each of the SCAs has two internal channels not connected to the input which can be used to correct for common mode noise and so-called fixed pattern noise due to charge loss in the capacitors (SCA-leakage). The sampling clock is supplied externally and can range from 1 MHz to 50 MHz. All the tunable parameters of the chip can be accessed via a custom serial slow control protocol.

Upon a trigger the content of the SCA is multiplexed to a differential line at a frequency of 20 MHz, time slice by time slice starting from the oldest sample. The full reading cycle takes 2 ms during which writing is disabled, which poses the main rate limitation of this chip.

### *7.3. Front-end card*

One front-end card (Fig. 29) houses four AFTER-chips and is directly connected to the pad plane via a 300-pin connector (SAMTEC BSH-EM-150) mounted sideways. Only 64 channels of the available 72 per chip are connected to the pad plane, such that one front-end card reads out a total of 256 detector channels. All four chips are controlled and read out in parallel. The total power consumption per card is 3.2 W. As the TPC is very sensitive to temperature variations, heat transfer from the front-end cards to the gas volume is avoided by dissipating the excessive heat with an active water-driven cooling system (see section 8). Figure 29 shows a photograph of a front-end card. Detector channels 1 – 32 are connected to the pins on the far side of the Samtec connector and thus have longer signal paths than detector channel 33 – 64, which are connected to the pins facing the Samtec connector (see also Fig. 45 in section 12.2).

### *7.4. Readout Chain*

For the read-out, the scheme developed for the COMPASS experiment [34] at CERN has been adapted for the GEM-TPC. The read-out scheme is displayed in Figure 30. Clock (38.88 MHz) and trigger signals are sent via optical fibers from the Trigger Control System (TCS) to readout driver modules (so-called GeSiCA) and from there they are distributed to the ADC modules. From there, each AFTER ASIC is supplied with two clock signals derived from the TCS clock: `WRITE_CLK`, which defines the sampling frequency and which is configurable as an integer division of a 77.67 MHz, and `READ_CLK`, which defines the data readout to the ADC and which is fixed to half the TCS clock (19.44 MHz). During the commissioning phase (cf. section 11, the detector was operated at an average trigger rate of  $\sim 140 \text{ s}^{-1}$ , determined



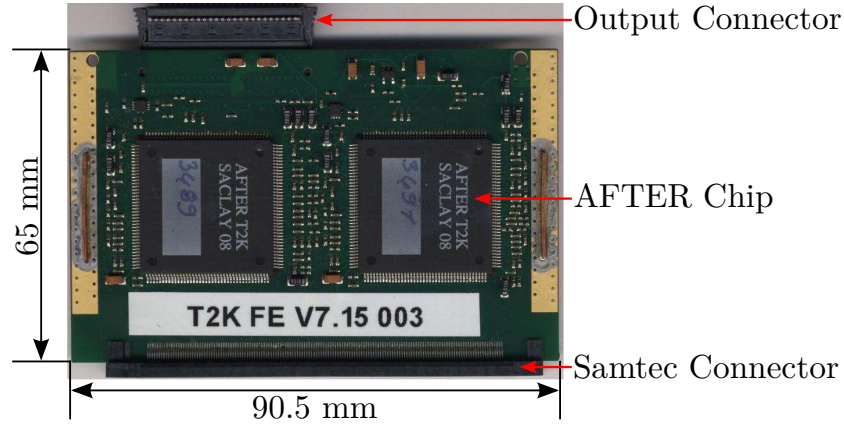


Figure 29: Photograph of the front-end card with two AFTER chips on each side. The Samtec connector is directly plugged to the backside of the pad plane. Each chip reads out 64 detector channels, 8 channels are not connected to the pad plane. The first 36 channels are connected to the pins of the ASIC on the far side from the Samtec connector, the second 36 to the ones on the near side. The backside of the card looks identical.

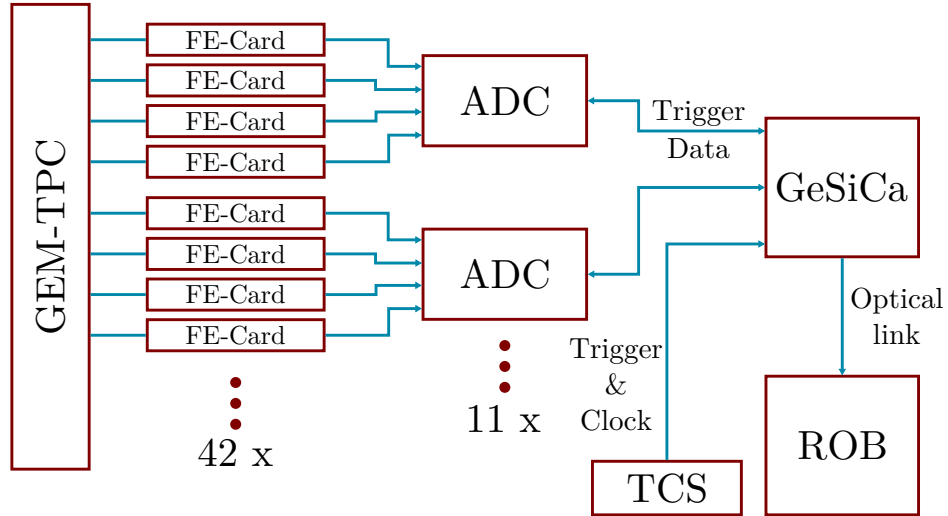


Figure 30: The GEM-TPC read out scheme. The signals from the GEM-TPC are sampled by the front-end (FE) cards and digitized by the analog-digital-converters (ADC). The ADCs send their data to the GEM-Silicon Control and Acquisition (GeSiCa) boards. Finally all data are collected in the read-out-buffer (ROB) computer. The trigger and clock is controlled by the Trigger Control System (TCS) and distributed via the GeSiCas to the ADCs and from there to the FE-cards.

mainly by the dead time needed to read out the buffer of the AFTER chip (cf. section 7.2). Upon arrival of a trigger signal the AFTER chips read the values stored in the SCAs and multiplex them via a differential line to the ADC modules. One ADC module can handle the data from up to four front-end cards (16 AFTER chips). The analogue signals from the AFTER ASICs are sampled by pipelined 12 bit ADCs with a sampling rate matching the readout clock of the AFTER ASIC. A Xilinx Virtex-4 FPGA on the ADC board performs online baseline subtraction and zero suppression of the digitized data. The zero suppression algorithm takes into account individual thresholds on each channel, calculated from the measured noise performance of the channels (see Sec. 12.2). To correct for the fixed pattern noise in the AFTER chip another correction algorithm has been implemented. For each channel of one SCA the mean of the two unconnected channels is subtracted to correct for the charge loss in the capacitors. After processing the data of 16 chips in the ADC module they are sent via an optical fiber to the GeSiCA module. One GeSiCA module can combine data from up to seven ADC modules and transmit these sub-events via an optical link to a read-out buffer at a maximum speed of 160 MB/s. The read-out buffer performs the final event building for the TPC and stores the data to a hard drive or sends it via TCP/IP to other computers for further processing. In total 42 front-end cards (168 AFTER chips) are used to read out the 10,254 channels of the GEM-TPC. This leads to a required number of 11 ADC and 2 GeSiCA modules. The total raw data size at the input of the ADC modules amounts to 9.8 MByte per event and corresponds to a data rate of 1.4 GByte/s at a trigger rate of  $140 \text{ s}^{-1}$ . After zero suppression in the ADC modules, the total data rate is reduced to  $\mathcal{O}(10 \text{ MByte/s})$ , depending on the occupancy and the duty cycle of the beam. For the experiment with a pion beam (cf. section 11), the average occupancy was 0.05% with a duty cycle of 53%, while for the tests with heavy-ion beams the occupancy was about 4 to 6 times higher with a similar duty cycle.

### 7.5. Gain Calibration of the AFTER-ADC System

The conversion gain of the system AFTER + ADC has been measured by injecting a known charge into a pin of the AFTER chip via a 1 pF SMD capacitor soldered to a readout pad of the pad plane. Several different amplitudes of a step-like input pulse have been used as shown in Fig. 31. The conversion gain derived from a linear fit is  $(0.063 \pm 0.003) \text{ fC/ADC channel}$ , or  $(393 \pm 19) e^-/\text{ADC channel}$ .

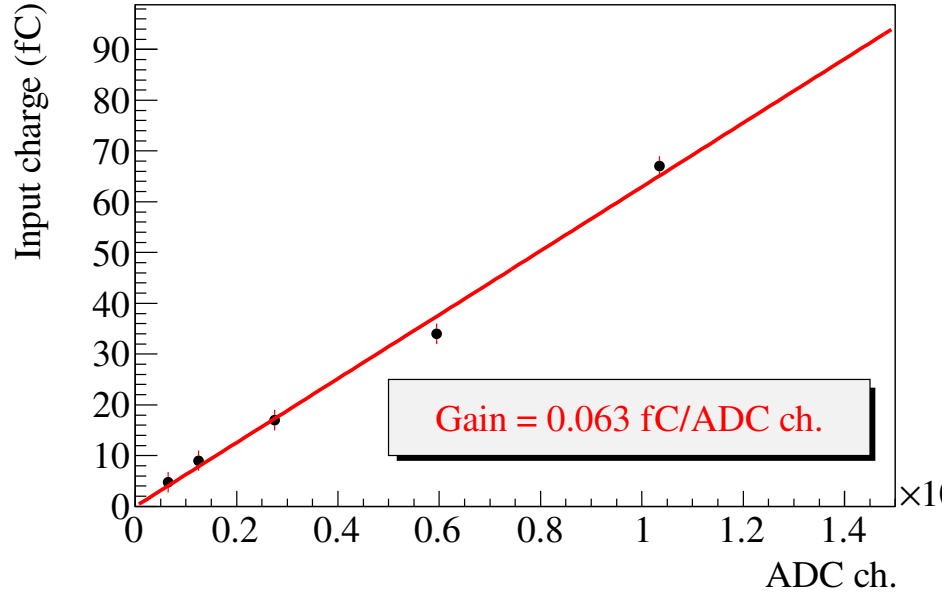


Figure 31: Gain calibration of the AFTER + ADC system for a peaking time of 116 ns and a charge range of 120 fC.

## 8. Cooling

With 7.5 mW power consumption per channel a total of 110 W created by all front-end cards has to be dissipated. Since the cards are directly plugged to the backside of the readout plane without a thermal barrier, it is important to actively cool the cards in order to avoid heat being introduced into the gas volume via the pad-plane, which would cause local variations of the drift velocity. In addition, cooling is needed for the ADC modules in order to avoid overheating of electronic components installed in regions without air convection. Both systems are cooled using a closed circuit water-driven cooling system operated at overpressure and connected to a chiller (Huber Kältemaschinen UC080T-H Umwälzkühler [35]). The latter provides a coolant temperature of 20 °C.

Each FE card is sandwiched between two copper plates put in direct contact with the four FE chips through heat conducting pads. The copper plates in turn are in contact with a heat exchanger connected to the cooling water circuit.

The FE cards are shown in Fig. 32 with the heat-conducting pads attached

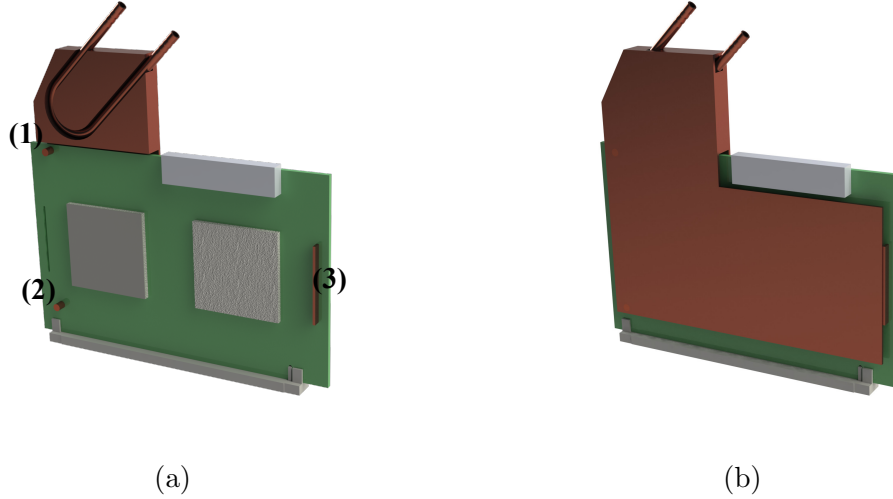


Figure 32: CAD rendering of one front-end card with its cooling components. Panel a) shows the front-end card with partially removed cooling system. One copper plate for heat transfer as well as one heat conducting pad between the copper plate and T2K chips (grey squares) has been removed. (1), (2) and (3) indicate the soldering positions of the copper plate. The front-end card with the complete cooling system attached is depicted in panel b).

to the housing of the FE chips shown in panel a) and with the copper plates attached to the pads as in panel b). The copper plates are mounted by soldering them at three positions 1-3 indicated in Fig. 32, panel a). The two pins (1-2 in Fig. 32, panel a)) are only soldered to the copper plates while the metal bar (3 in Fig. 32, panel a)) is also soldered to the PCB. The heat exchanger is mounted by three screws to the copper plates. This way, the heat exchanger can be removed and this allows for an easy mounting of the FE cards. The pipe for the cooling water is soldered into a groove in the copper block and has an outer diameter of 3 mm and a wall thickness of 0.5 mm. Since 42 FE cards have to be cooled at the same time, a homogeneous flow of cooling water through all heat exchangers has to be guaranteed. This was achieved by attaching inlets and outlets, one pair for each FE card, to the supply line such that the flow resistance is the same through all heat exchangers. The scheme in Fig. 33 shows how this is realized. One can see that the path length and therefore the flow resistance of the cooling liquid is the same for each heat exchanger. The cooling water is distributed by two rings

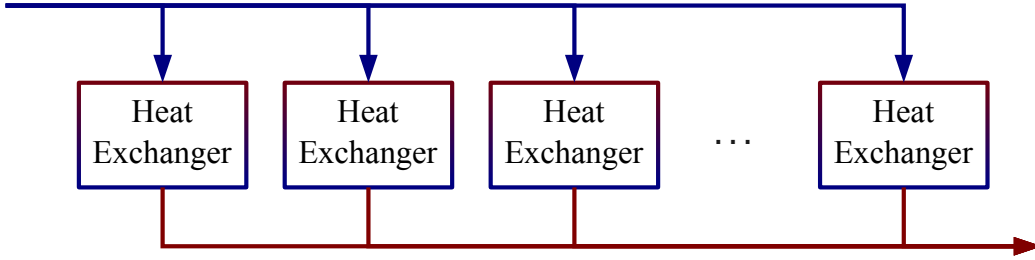


Figure 33: Scheme of the cooling distribution.

made out of copper pipes to allow for soldering nozzles for the connection to the FE card heat exchangers by flexible polyurethane tubes. Figure 34(a) shows a CAD rendering of the complete cooling setup as it was used for the GEM-TPC. To validate the uniformity of the cooling, simulations were taken

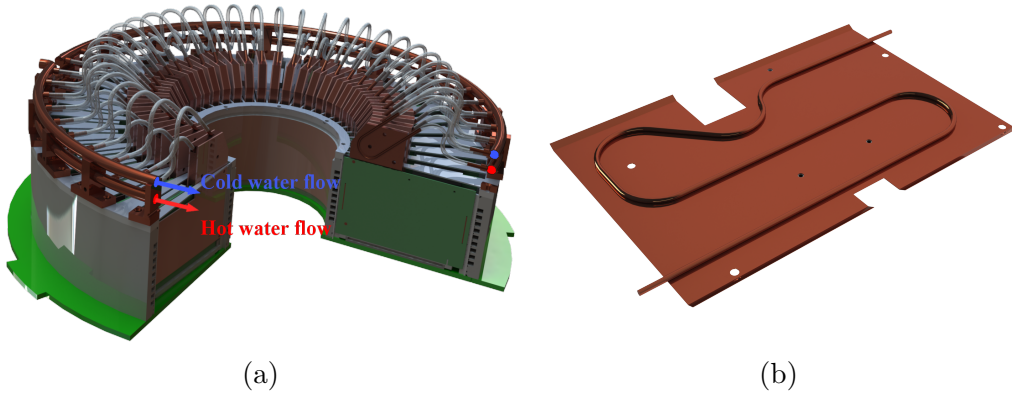


Figure 34: Panel a): CAD rendering of the complete cooling setup. For a better visibility a quarter of the setup has been cut away. Panel (b) shows a CAD rendering of the ADC cooling sheet metal.

out in two steps. In the first step the flow of the cooling liquid including the heat exchangers but not the FE cards were simulated. The second step was the simulation of the heat distribution in the FE cards taking the results of the first step into account.

The simulation for the first step was performed with the FEM flow simulation framework of SolidWorks. It was found that taking into account an inlet water flow of  $50 \text{ ml s}^{-1}$  the flow of the cooling liquid through the heat exchangers

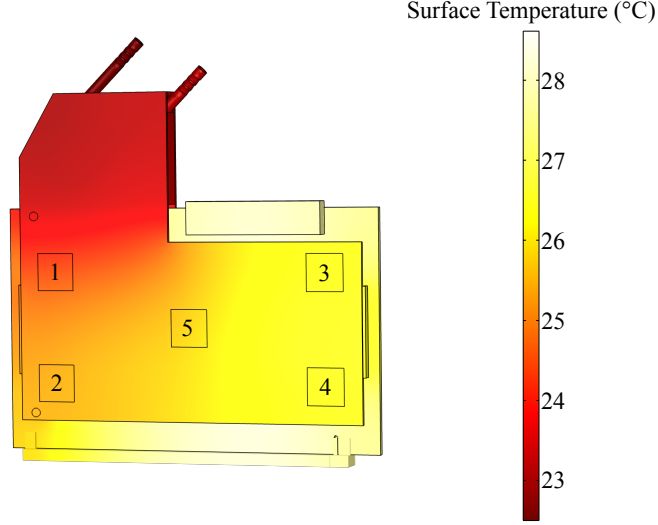


Figure 35: Simulated surface temperature distribution of one FE card. The 5 rectangles indicate the measurement positions.

is in average  $1.1 \text{ m}\ell\text{s}^{-1}$  with a still rather large variance of  $0.56 \text{ m}\ell\text{s}^{-1}$ . As mentioned above, in a second step the temperature distribution of the FE card was calculated for all 42 liquid flow values found in the previous simulation. This calculation was carried out using the COMSOL FEM software and the model shown in Fig. 34. Each chip introduces a power of  $0.625 \text{ W}$  uniformly on its surface and only heat transport by conduction through the FE card and cooling system materials is assumed. The model was validated beforehand by a measurement showing that the maximal difference between measurement and calculation is below  $0.6^\circ\text{C}$ . Figure 35 shows the outcome of this calculation where a flow of  $1 \times 10^{-5} \text{ m}\ell\text{s}^{-1}$  and a water temperature of  $22.5^\circ\text{C}$  were used for the calculation. Finally, an average temperature of  $21.3^\circ\text{C}$  with a variance of  $0.25^\circ\text{C}$  measured at position 5 in Fig. 35 was found for the FE cards taking into account the various flow values from the calculation mentioned above and a water temperature of  $18^\circ\text{C}$ .

The same system provides the cooling of the voltage regulators of the ADCs and the ADCs themselves through a serial connection of the pipes following the cooling ring for the FE cards. In this case, a copper sheet with an soldered pipe was attached to each ADC module (Fig. 34(b)). In the same

way as for the FE cards each chip was in thermal contact via an heat conducting pad with an aluminium block which again was screwed to the copper sheet. The bending of the pipe in contact with the copper sheet was chosen to maximize the contact area and to cross each aluminium block.

## 9. Gas System

### 9.1. Operational Requirements

The gas system supplies the detector vessel with the drift gas mixtures Ar/CO<sub>2</sub> (90/10) and Ne/CO<sub>2</sub> (90/10) and with a radioactive Kr gas during calibration. In order to test different gas mixtures the system must be capable of switching between gases and modifying the mole ratio to test different quencher contributions. The system also must allow the user to change the detector gas to nitrogen during stand-by mode in order to keep the detector volume dry and oxygen-free.

One of the main requirements to the GEM-TPC gas system is the minimization of the oxygen and water vapour concentration inside the detector vessel. A contamination by an electro-negative gas as O<sub>2</sub> leads to attachment of the primary electrons and thus to a deterioration of the spatial and  $dE/dx$  resolution. The water vapour reduces the effective drift field and the drift velocity since H<sub>2</sub>O molecules can be easily polarized shielding the electric field. A contamination by oxygen or water vapour can originate from badly sealed joints and permeation through the TPC wall material. For the large ALICE TPC, where the volume-to-surface ratio is about 0.7 m, an oxygen level lower than 5 ppm was reached. This value can be considered as a reference for this GEM-TPC where the volume-to-surface ratio is only 0.1 m. In addition to the gas purity, the accuracy and stability of the CO<sub>2</sub> content is crucial, as it determines important parameters like the drift velocity and diffusion within the gas.

### 9.2. Implementation

A closed gas circulation system is employed for the GEM-TPC (see Figure 36). The system is composed of a mixing unit, a flow control unit, and a pressure control unit. For the mixing of the gas two SLA5850S mass flow controllers (MFC) are used. By regulating the gas flow of the individual mass flow controllers the desired mixing ratio of Ar/Ne and CO<sub>2</sub> is achieved. The gas mixture is filled into a 12 ℓ buffer volume which serves as a reservoir to refill the gas system if needed. During operation the pressure inside the

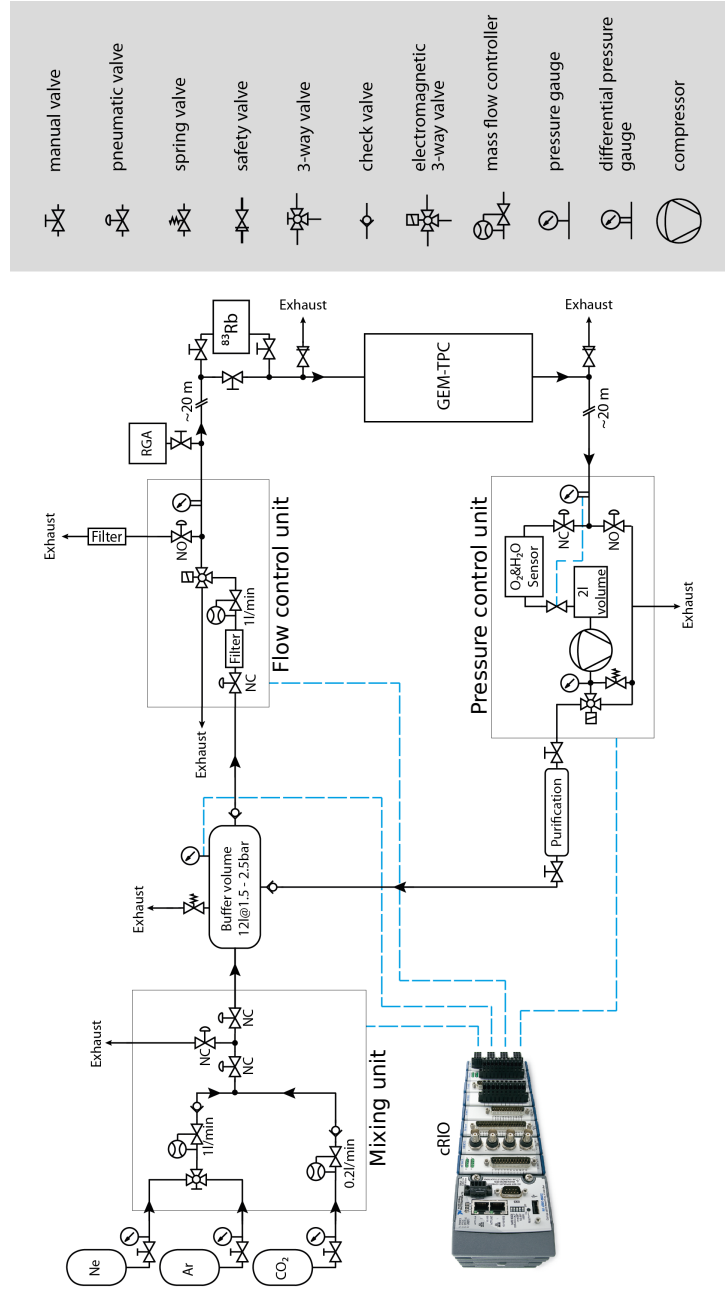


Figure 36: Flow chart of the gas system for the GEM-TPC. The symbols are explained in the legend on top; NC/NO is shorthand for normally closed/open; residual gas analysis (RGA) is performed using a quadrupole mass spectrometer (QMS). Black lines indicate stainless steel or copper pipes, blue lines electrical connections.



buffer volume is kept between 1.5 and 2 bar. One of the outputs of the buffer volume is connected via a 10  $\mu\text{m}$  particle filter to the flow control unit which controls the total gas flow to the TPC. The total volume of the GEM-TPC is about 45  $\ell$  and a flow rate of 45  $\ell\text{ h}^{-1}$  is used for both Ar/ $\text{CO}_2$  and Ne/ $\text{CO}_2$  gas mixtures. A differential pressure gauge is installed in the flow control unit to measure overpressure up to 100 mbar. A residual gas analyzer (RGA) is installed in order to monitor the gas composition after the flow control unit using a quadrupole mass spectrometer (QMS). Figure 37 shows an example of this measurement for a time interval of 2.5 days. The ratio Ar to  $\text{CO}_2$  is shown for the analyzed gas sample and a calibration sample composed of a premixed Ar/ $\text{CO}_2$  gas. The measured  $\text{CO}_2$  concentration with an error band corresponding to 1% fluctuations is shown as well.

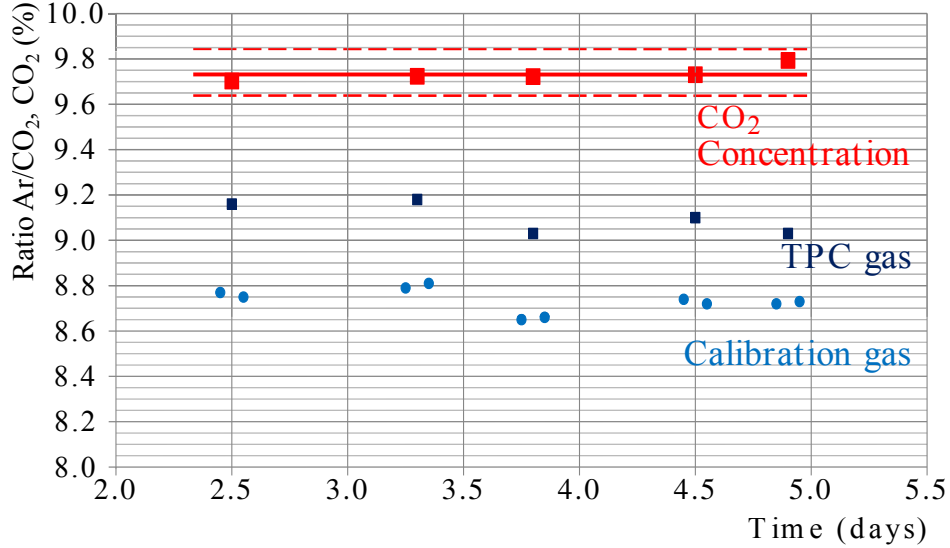


Figure 37: QMS (quadrupole mass spectrometer) analysis of the  $\text{CO}_2$  content in an Ar/ $\text{CO}_2$  (90/10) gas mixture over 2.5 days of data taking.

For calibration of the gain uniformity (see section 12.3), radioactive  $^{83\text{m}}\text{Kr}$  can be introduced into the TPC by flushing the gas through a vessel containing  $^{83}\text{Rb}$ . A pressure control unit is located at the gas outlet of the TPC. This unit controls the total overpressure and measures the oxygen and water vapour content of the gas. For the oxygen measurement a Teledyne Model 3190 system with a measurement range from 0 ppm to 100 ppm and a relative accuracy of 2% was used. In Fig. ?? the oxygen content for a period of five

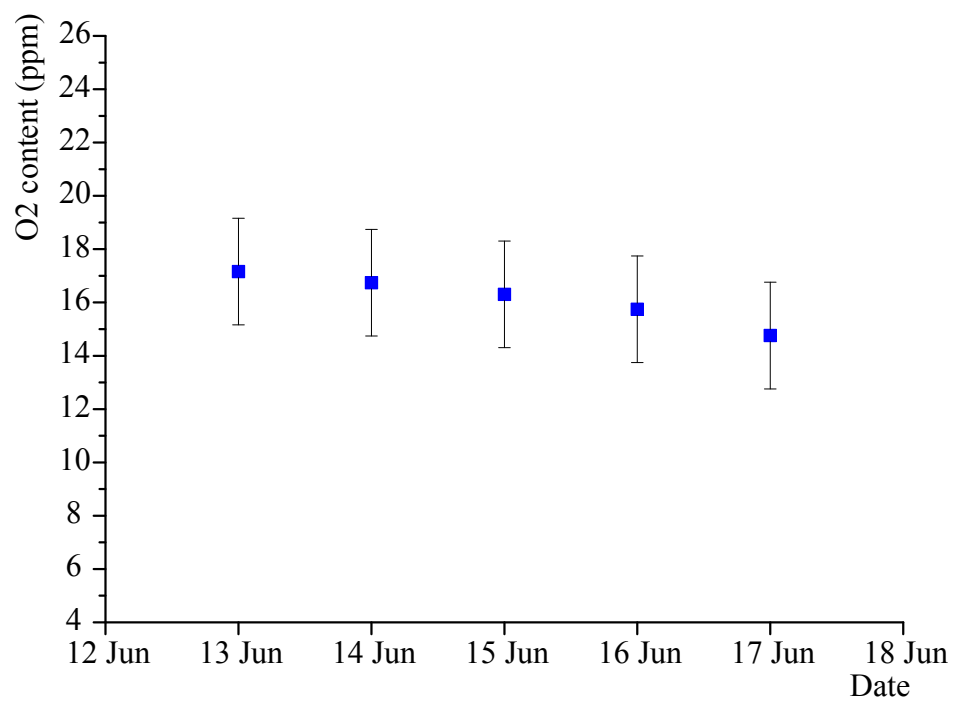


Figure 38: Development of the mean oxygen content over a period of five days.

days is shown. The mean oxygen content within this time drops slightly from 17 to 15 ppm. This still rather large number is probably due to leakages in the field cage sealing but it did not lead to any significant signal losses. To measure the water vapour content a EE375 dew point transducer was used. After leaving the pressure control unit the gas enters the purification to remove oxygen and water vapour from the gas. The oxygen is removed with activated copper by oxidizing to copper-oxide while the water vapour is removed by molecular sieves with a pore size of 3 Å. The whole gas system is controlled by a National Instruments CompactRIO module which consists of:

- a NI-9265 current output module to control the set points of the MFCs,
- a NI-9203 to read the MFC output signals,
- a NI-9205 to read the outputs of the pressure gauges, the oxygen sensor and the water vapour sensor,
- a NI-9237 to read out the pressure gauge of the flow control module,
- Two NI-9485 to control the electromagnetic three-way valves.

All valves and flow MFCs were controlled by a LabView-based slow control system which also monitored and recorded all values. Further details about the gas system can be found in [36].

## 10. Slow Control System

For a safe detector operation it is crucial to monitor and control all parameters in a convenient and reliable way. In the case of the TPC the main parameters to be controlled are the high-voltage potentials of the cathode, the last strip, and the GEM foils and the low voltage of the front-end powering. Furthermore various temperature and pressure sensors located inside the TPC have to be monitored.

### 10.1. High-Voltage System

A safe operation of the TPC requires a supervision of every individual high voltage that is applied to the GEM foils and the drift cathode. In addition, the possibility to operate all high voltage channels simultaneously, especially during ramping, is required. To avoid any damages to the chamber, a fast

emergency shutdown of the high voltage system is indispensable. Furthermore the system should allow the configuration of this emergency shutdown. The high voltage system for the GEM stack requires a voltage stability below 50 mV, current measurement with a resolution of  $\approx 1$  nA, adjustable ramp speeds, full remote controllability and output voltages of up to 6 kV. For the drift cathode a high voltage system with a voltage of up to 30 kV and currents up to 1 mA is needed. An ISEG EHS 8060n HV module and an ISEG HPn300, controlled by a W-Ie-Ne-R MPOD crate were employed as this modules satisfy all demands. Both systems have a fast hardware based over-current trip switch with a channel-wise adjustable current limit and they can be controlled via Simple Network Management Protocol (SNMP) commands over Ethernet or directly over CAN bus.

The current architecture of an emergency high voltage shutdown system offers two solutions. A purely hardware-based approach and a hardware plus software approach. The hardware approach couples the HV system of the cathode and the field-cage with the HV system of the GEM stack by an interlock cable. In case of a trip in one of the two systems both are shutdown immediately. In this scenario a trip in the GEM stack also causes the drift voltage to trip and vice versa.

The long ramping time of the cathode after such a trip introduces hereby a significant dead time of several hours. For the hardware plus software approach the HV systems are not coupled by an interlock cable and therefore trip independently. To minimize the the potential danger of sustained discharges between the first GEM foil and the last field-cage strip in case of a trip of the GEM stack, a software adjustment of the drift cathode voltage to 60 % of the nominal value is implemented. In case of a trip of the cathode HV no additional actions have to be taken. Besides the trip behavior, two additional security functions are implemented: if the measured voltages rises above a threshold voltage or if the current steps up unexpectedly the TPC is ramped down with  $100 \text{ V s}^{-1}$  to prevent severe damages. The moving average over the last 10 values is calculated continuously and compared with the set value. If the deviation is larger than the limit an alarm rings. The limit can be adjusted via the slow control interface (section 10.3) with a default value of 5 % of the set voltage of the respective channel.

To detect over-currents, the average of the last ten measured values is compared with the average of ten values from ten seconds earlier. Especially the currents are good indicators for a possible failure of the detector, because any short-cut between the GEM foils or at the field-cage will result in a sudden

increase of the current. The default for the over-current check is an increase of the current by a factor of 1000. This value can also be configured via the slow control interface. It has been found that this check is only necessary during the ramping. As soon as the desired potentials are reached the hardware over-current protection of the high voltage modules is preferable as it is much faster.

### *10.2. Temperature, Pressure and Gas Flow*

Various sensors are directly attached to the TPC, namely temperature sensors on the pad-plane and the outside field-cage walls and gas flow and pressure sensors. For the temperature measurement at the outer surface of the TPC 210 Dallas 18B20U 1-wire temperature sensors are used. The 12 PT100 temperature sensors located on the pad-plane are digitized by AD7998 12-Bit ADCs and read out via an Ethernet-to-I<sup>2</sup>C adapter. The ASF1400 gas flow sensor is read out via RS232 while the pressure sensor is read out by a custom-made ATmega32 based read out.

### *10.3. User Interface*

The control and read out of the high voltage modules, temperature, flow and pressure sensors is realized by a C++ based graphical user interface (GUI). In order to communicate between the GUI and the high voltage modules a background daemon is used. Additionally all data such as the actual voltages are collected by this daemon and written to a SQL based database where they are saved with a time-stamp in order to associate them to the detector measurement data files and for a later use during the data analysis. The GUI directly accesses this database to display all recent values. Furthermore it is used to calculate all needed electric potentials from user defined electric fields and potential differences across the GEMs (Fig. 39 upper part) taking into account a linear scaling factor (Fig. 39 upper right area). If all values are set the ramping of all channels to the desired values with given ramp speeds can be started from the GUI. The lower part of the interface display is mainly to monitor the crucial voltages and currents. There is also the possibility to change specific settings such as trip limits, or ramping speeds for all or single HV channels. Further details concerning the slow control system can be found in [37].

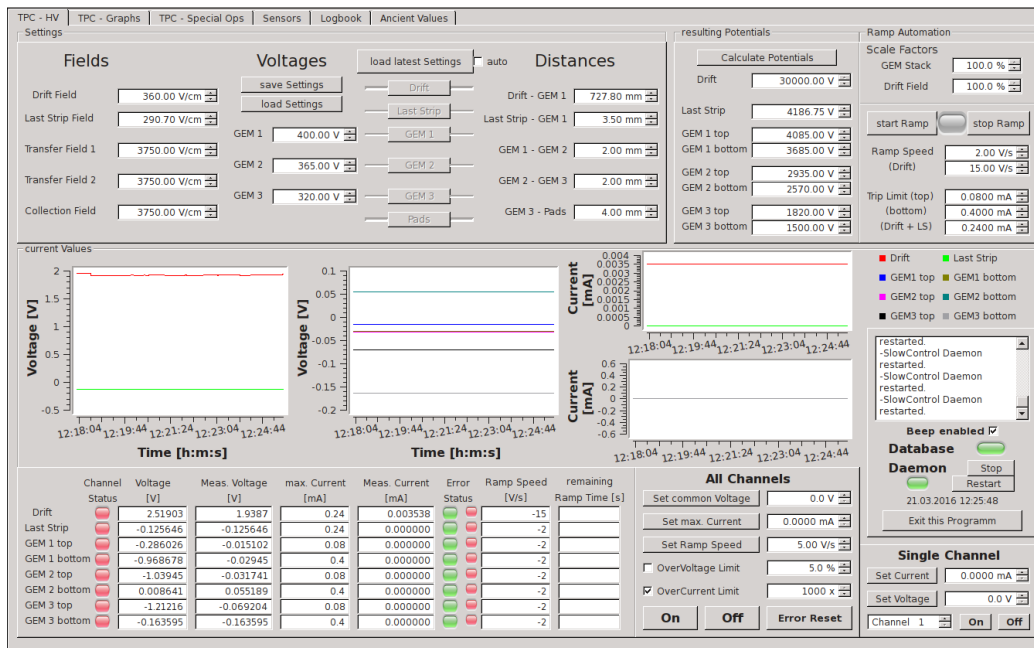


Figure 39: Screenshot of the slow control user interface. For details see text.

#### 10.4. Low-Voltage System

Besides the high voltage also the low voltage of the 42 front-end cards as well as the 11 ADCs has to be controlled. The low voltage for both systems is supplied by two pairs of Agilent 6031a and two pairs of Agilent E3634 power supplies which are controlled by a LabView based slow control software. To communicate with the GPIB based power supplies a GPIB-to-Ethernet converter is used. The power supplies are floating with their ground being defined by the detector to avoid ground loops. In order to distribute the low voltage to the individual front-end cards and ADCs break-out-boxes are used. The sense wires for measuring the actual voltage are placed inside these boxes.

### 11. Commissioning at the FOPI spectrometer

To test the performance of the large GEM-TPC it was installed inside the FOPI [27] experiment at GSI (Darmstadt, Germany), a large-acceptance spectrometer designed to study the properties of compressed nuclear matter produced in heavy-ion collisions at energies from 0.1 AGeV to 2.0 AGeV. The detector system has an almost complete azimuthal symmetry and nearly  $4\pi$  coverage of the solid angle. It consists of a central drift chamber (CDC), a scintillator barrel, and resistive plate chambers (RPC) arranged cylindrically around the target. The setup is operated inside a 0.6 T superconducting solenoid magnet. The barrel part is augmented by a system of forward detectors including a planar drift chamber (Helitron) and a plastic scintillator wall (PLAWA). The GEM-TPC was mounted inside the inner bore of the CDC, supported only on the upstream side at the media flange by a light-weight ring-shaped structure made of carbon fiber. A schematic cross-section of all FOPI barrel sub-detectors, including the TPC, is shown in Fig. 40. Figure 41 shows a three-dimensional model of the FOPI barrel system. FOPI is able to identify light charged particles like pions, kaons and protons and intermediate mass fragments. Hadron resonances and neutral hadrons can also be reconstructed from their decay products.

Before the installation of the GEM-TPC, the FOPI spectrometer delivered a vertex resolution of about 5 mm in the  $x - y$  plane and 5 cm along the beam axis. The momentum resolution for charged particles was 4 % - 10 %. The motivation to install the GEM-TPC in FOPI was threefold: (i) the barrel detectors provided a full-fledged magnetic spectrometer and thus an ideal reference environment to test the GEM-TPC in different beams including

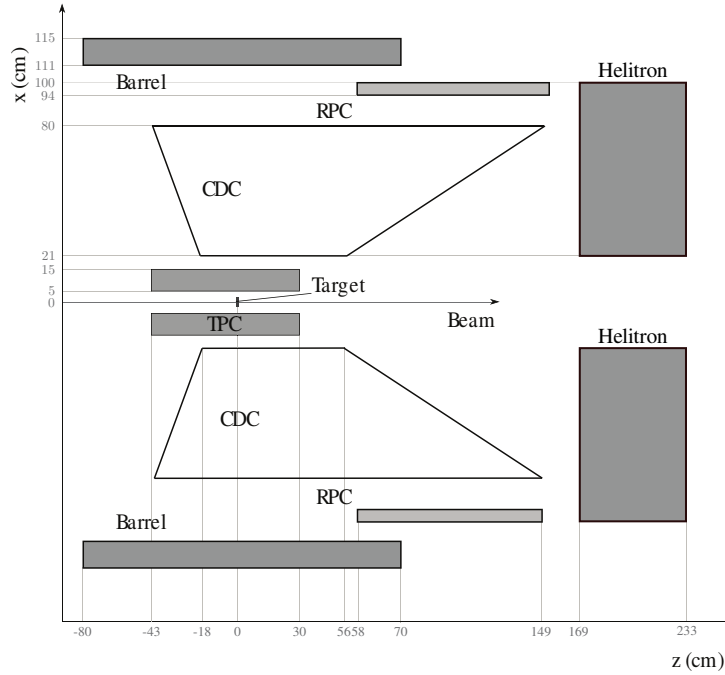


Figure 40: Schematic view of the sub-detector arrangement within the FOPI spectrometer.

heavy-ion interactions, (ii) the GEM-TPC was expected to improve substantially the vertex and secondary vertex resolutions of the spectrometer, and (iii) with its large geometrical acceptance covering both barrel and forward detectors, the GEM-TPC was supposed to improve the inter-connection between these different sub-detector elements.

The commissioning and operation of the GEM-TPC installed in FOPI was done in several phases. In the first phase, which started in October 2010, the TPC was commissioned with cosmic muons without and with the solenoid magnetic field. Data with cosmic muons were also taken in 2011 and 2012 for more detailed studies of the detector performance [30], which will be reported on in a forthcoming publication. In the second phase the stability of the GEM-TPC in collisions of different heavy-ion beams with nuclear targets was tested in November 2010 and April 2011. The third phase consisted of a three-week period of stable operation of the GEM-TPC during the FOPI S339 physics campaign in June 2011 with a 1.7 GeV/c pion beam impinging on solid targets. For this secondary beam only a rate of 25.000  $\pi^-$ /spill with a total spill length of 3.5 s and a duty cycle factor of 42 % was available.



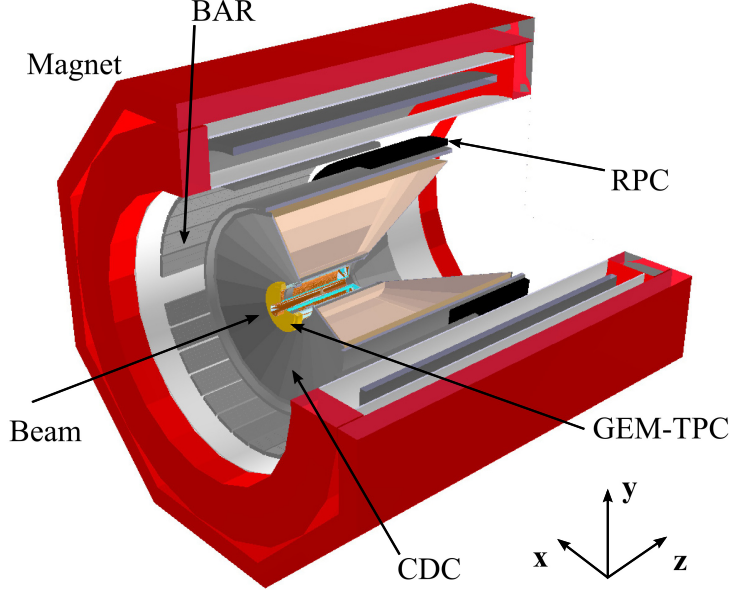


Figure 41: Model of the barrel part of the FOPI spectrometer showing, with increasing radial distance from the beam axis, the GEM-TPC, the central drift chamber (CDC), the resistive plate chambers (RPC), the scintillator barrel (BAR), and the 0.6 T solenoid magnet.

The major aim of this experiment was to measure charged and neutral kaons produced almost at rest in a nuclear medium. The data taken during this period resulted in the first measurement of the specific energy loss over a wide momentum range with a large GEM-TPC [38]. The physics results from this beam time [39] will be the subject of a forthcoming publication.

During the first two phases, two different gas mixtures, Ar/CO<sub>2</sub> (90/10) and a Ne/CO<sub>2</sub> (90/10), and several different field configurations were tested, both for the drift field and for the GEM stack. For the GEM stack, two categories of settings were used: the *Standard Setting*, optimized for stable operation in hadron beams and derived from the COMPASS experiment [13], and the so-called *Ion Backflow Settings*, which were found to minimize the ion backflow in a triple-GEM setup [40]. The values for the fields and GEM potential differences corresponding to these two categories for a gas gain of  $\sim 1 \cdot 10^4$ , respectively, are displayed in Table 5. Since the GEM-TPC is normally operated at a lower gain of  $1 - 2 \cdot 10^3$ , all potentials except the drift field are scaled down from the values given in the table by an overall scaling

factor.

	Standard Setting		Ion Backflow Setting	
Drift Field	400	$\text{V cm}^{-1}$	250	$\text{V cm}^{-1}$
$\Delta U_{\text{GEM1}}$	400	V	330	V
$E_{\text{trans1}}$	3750	$\text{V cm}^{-1}$	4500	$\text{V cm}^{-1}$
$\Delta U_{\text{GEM2}}$	365	V	375	V
$E_{\text{trans2}}$	3750	$\text{V cm}^{-1}$	160	$\text{V cm}^{-1}$
$\Delta U_{\text{GEM3}}$	325	V	450	V
$E_{\text{Ind}}$	3750	$\text{V cm}^{-1}$	5000	$\text{V cm}^{-1}$

Table 5: Standard and Ion Backflow settings for drift field and GEM amplification system. See Fig. 24 for a sketch of the HV powering scheme of the GEM-TPC.

- Several drift fields have been applied: 150, 200, 300 and  $360 \text{ V cm}^{-1}$  with the corresponding drift velocities: 0.9, 1.4, 2.2 and  $2.9 \text{ cm } \mu\text{s}^{-1}$  [41].
- Different voltage settings for the GEM-stack resulting in different gains have been tested ranging from 80 % to 100 %.
- Two gas mixtures, namely Ar/ $\text{CO}_2$  and Ne/ $\text{CO}_2$  have been used, both in a 90/10 mixture by weight.

The third phase (physics campaign) was conducted with the Ar-based gas mixture at a drift field of  $234 \text{ V/cm}$  and a GEM gas gain of  $\sim 1 \cdot 10^3$  achieved at a scaling factor of 81% of the standard GEM settings (second column in Table 5).

#### 11.1. Tracks from Cosmic Muons

In the first phase, tracks from cosmic rays were measured using the scintillator barrel of FOPI as a trigger. Figure 42 shows the online event display for a typical cosmic muon track traversing the chamber and producing additional  $\delta$ -electrons. This event was registered without a magnetic field and with the following settings for the TPC: a drift field of  $360 \text{ V cm}^{-1}$  with an Ar/ $\text{CO}_2$  (90/10) mixture, which translates into a drift velocity of  $\approx 2.9 \text{ cm } \mu\text{s}^{-1}$ , and a GEM potential scaling factor of 85 % for standard settings. Various drift, gain, and gas settings were measured with cosmic muons in order to get a comprehensive picture of the detector performance, especially in terms of spatial resolution.

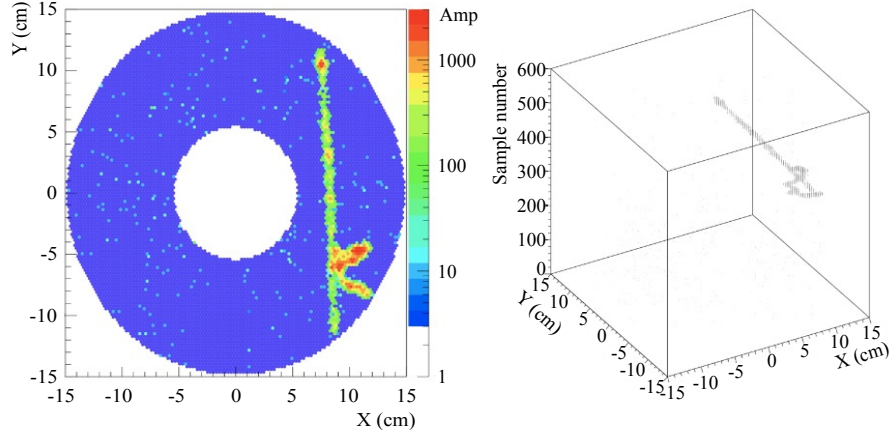


Figure 42: Online display of a cosmic muon track producing two  $\delta$ -electrons in the GEM-TPC. The left panel displays the signal amplitudes registered on the electrodes of the pad plane in units of ADC channels, i.e. the 2-D projection of the track. The right panel shows the full 3-D spatial information with the sample number on the z-axis.

### 11.2. Tracks from Beam Interactions

Several beam species were utilized to collect data for the joint GEM-TPC/FOPI system during two test experiments at GSI in November 2010 and April 2011:  $^{84}\text{Kr}$ ,  $^{197}\text{Au}$  and  $^{22}\text{Ne}$  beams at 1.2 AGeV, 1.0 AGeV, and 1.7 AGeV kinetic energies, respectively, impinging on an Al target with 2 % of a nuclear interaction length placed in the inner bore of the GEM-TPC. The beam parameters were set to an average particle rate of  $5 \cdot 10^6$  particles/spill with a total spill length of about 10 s and a duty cycle factor of 50 %.

Figure 43 shows two typical events in the GEM-TPC for  $^{22}\text{Ni}+\text{Al}$  reactions. The chamber settings during this test were  $360 \text{ V cm}^{-1}$  drift field in the Ar/CO<sub>2</sub> (90/10) mixture and a GEM scaling factor of 86 % for standard settings. The top row shows an event where the beam particle presumably interacted upstream of the target, producing tracks almost parallel to the beam axis and several low-momentum particles curling in the 0.6 T magnetic field. In the bottom row an interaction in the Al target is displayed which produced a large number of charged particles.

These online event displays provide direct evidence for the excellent 3-D tracking capability of a TPC, where the large density of hits along a particle track facilitates pattern recognition even in high-multiplicity events. Figure 44 shows the track multiplicity, i.e. the distribution of the number of reconstructed tracks per event, in the GEM-TPC for  $^{22}\text{Ne}+\text{Al}$  collisions at

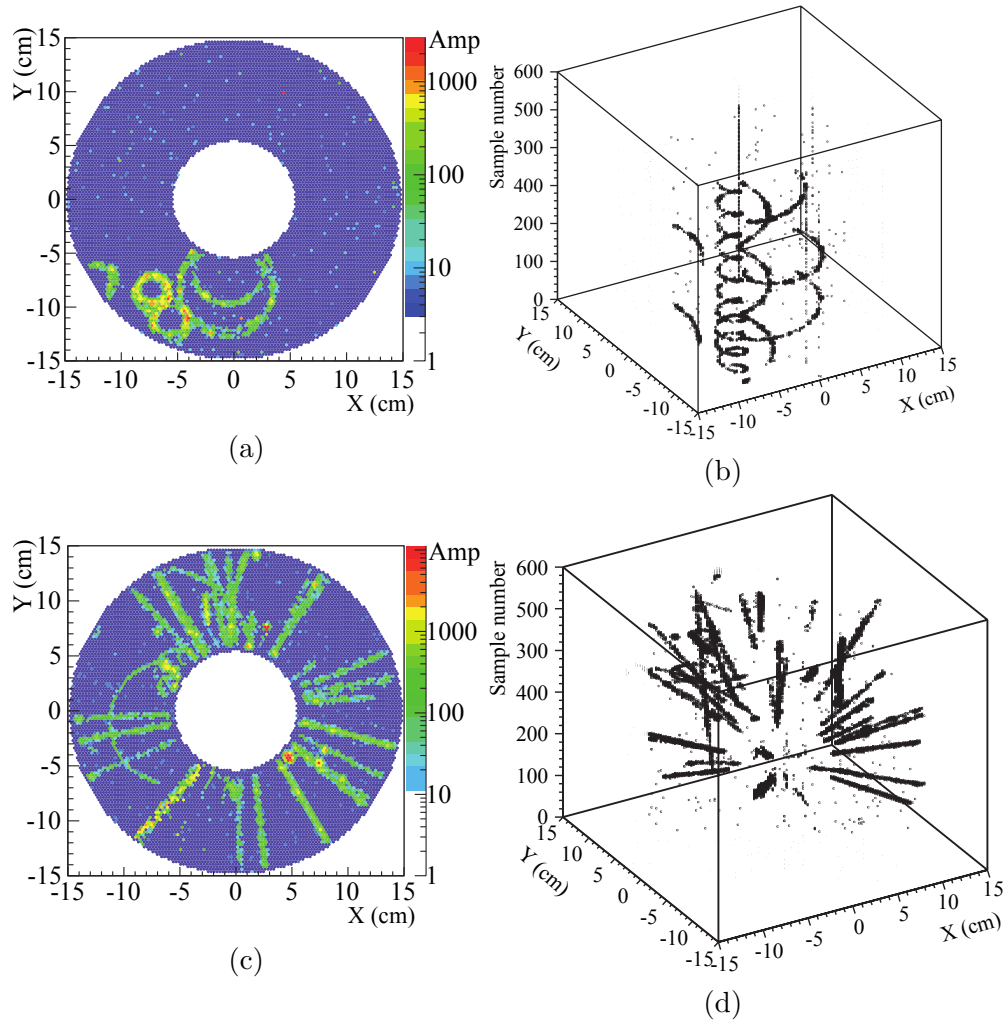


Figure 43: Online displays from the test with  $^{22}\text{Ne}$  ions with 1.7 AGeV. The left panels shows the signal amplitudes registered on the readout pads in units of ADC channels, the right panels the full 3-D information with the sample number on the  $z$ -axis. In the top row, an event is displayed where the beam ion presumably interacted upstream of the target and produced several low-momentum particles curling in the magnetic field. The bottom row shows a high-multiplicity event from an interaction of the beam in the Al target.

1.7 AGeV. As one can see, events with up to 100 tracks were successfully reconstructed.

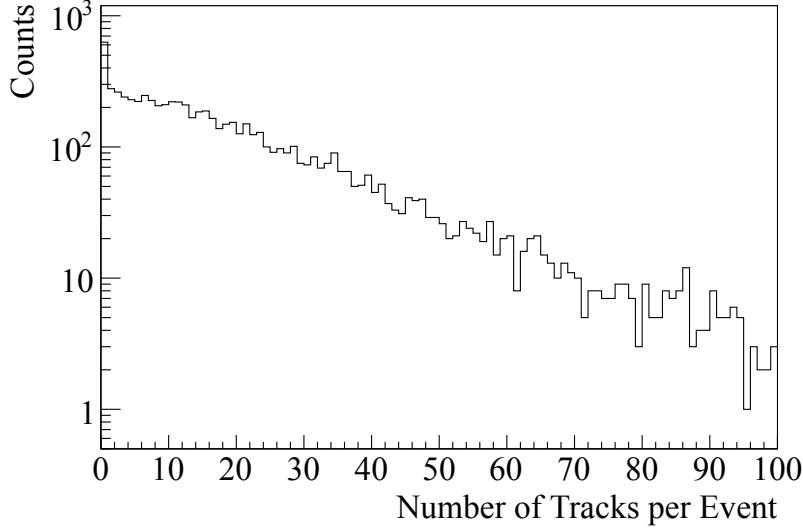


Figure 44: Track multiplicity distribution of the reconstructed events in the GEM-TPC detector for  $^{22}\text{Ne}+\text{Al}$  collisions at 1.7 AGeV.

For track fitting, the track segments in the TPC with an average length of 14 cm are combined with the longer segments in the CDC. This allows the determination of particle momenta exceeding 1 GeV/ $c$ , for which the curvature in the GEM-TPC alone is too small.

## 12. Calibration procedures

A TPC requires a number of calibration procedures to be performed at regular intervals in order to achieve the design performance. For the GEM-TPC, the following calibration steps were implemented and applied:

- pedestal and noise determination,
- gain determination and equalization,
- drift velocity calibration.

They will be described in the following subsections.

While the first procedure is done on a sample-by-sample basis for each channel separately, the other two require a reconstruction of signals from the digitized data. The full set of algorithms to reconstruct particle tracks in the

TPC will be described in a forthcoming publication ; here, we limit ourselves to the description of the algorithms to generate so-called *reconstruction clusters*, or simply *clusters*, which then also provide the input for the tracking algorithms.

### 12.1. Cluster Reconstruction

As a first step, consecutive samples of each pad with amplitudes above a given threshold are combined to so-called *pad hits* by using a simple pulse shape analysis (PSA) technique. Samples belonging to one pulse are identified by a search for local minima. The pad hit gets assigned a total signal charge (the sum of all associated sample amplitudes above threshold) and a signal time (time of the peak sample minus a constant offset of 149.5 ns which takes into account the rise time of the signal). In the second step, accumulations of pad hits in 3-D space are further compressed into clusters in order to reduce the amount of data and further suppress noise hits. The clustering procedure starts from the pad hit with the highest amplitude in a given drift frame and adds pad hits both from neighboring pads on the pad plane and along the drift direction if they are sufficiently close in time. The hit association to a given cluster stops at local minima of the hit amplitude and a new cluster is started at the remaining pad hit with the highest amplitude until all pad hits are taken into account. Then a cut is applied on clusters consisting of only one pad hit, which effectively removes electronic noise hits. The total amplitude of a cluster is given by the sum of the amplitudes of the associated pad hits, its position is calculated as the center of gravity of the associated pad hits.

### 12.2. Pedestal and noise determination

In order to cope with the large amount of data from the TPC, noise hits are suppressed already during data taking after digitization in the ADC, as described in Sec. 7.4. The zero suppression logic is implemented in a Xilinx Virtex-4 FPGA on the ADC card and consists of baseline (pedestal) subtraction with individual values for each channel, common mode and fixed pattern noise correction for all channels connected to one side of the chip packaging, and suppression of all channels with amplitudes smaller than a threshold defined by a programmable multiple (typically between 3 and 5) of the individual noise value of the given channel.

The pedestal and noise values for each channel are determined in regular so-called pedestal runs. In these runs, which are performed at nominal chamber

conditions but without beam, a random trigger is used to read out a small number of samples of each channel without zero suppression. The number of samples per channel is limited to typically 6–10 by the bandwidth of the readout chain. From this data sample, the average (pedestal) and the rms width (noise in ADC channels or equivalent noise charge, ENC, if converted to charge) of the recorded baseline values are determined offline for each channel and saved in a file. The values in the file are then uploaded to the ADC card using the I2C protocol and applied to the raw data when zero suppression is activated.

The noise values of all channels of one front-end chip can be seen in Fig. 45 (left). The distribution of the noise values for all 10254 channels connected to the pad plane is shown in Fig. 45 (right). There are two groups of channels with a slightly offset noise distribution, related to the signal paths on the front-end card. The first 36 channels of each chip have longer input lines than the second 36 channels. This reflects in a slightly different noise level of these groups of channels, as can be seen from Fig. 45. The outlier channels with higher noise are typically the ones on the edges connected to the far side of the chip pins.

The average noise (including the tails) of all channels is 1.83 ADC channels,

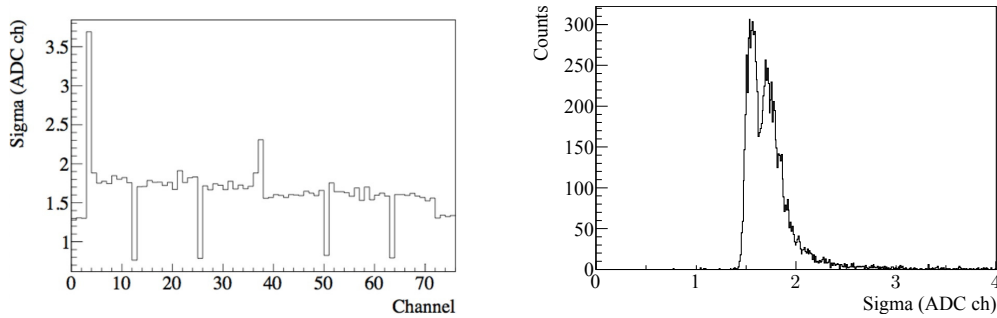


Figure 45: Left panel: noise values in ADC channels for all 76 channels of one front-end chip connected to the GEM-TPC. The first and the last four channels are not connected to the pad plane. The four intermediate low-noise channels are used for the correction of fixed-pattern noise caused by leakage of the switched capacitor array. The first 36 channels have longer input lines on the front-end cards (see Fig. 29) and a correspondingly higher noise. Right panel: distribution of the noise values for all connected channels of the GEM-TPC.

corresponding to an equivalent noise charge of  $720 e^-$ . The most probable values of the ENC for the two groups of channels are  $616 e^-$  and  $674 e^-$ , for

input capacitances of 13 pF and 16 pF, respectively. Figure 46(a) shows the pedestals values for all pads of the pad-plane in units of ADC channels, while Fig. 46(b) displays their noise values. The ring structure with a higher noise

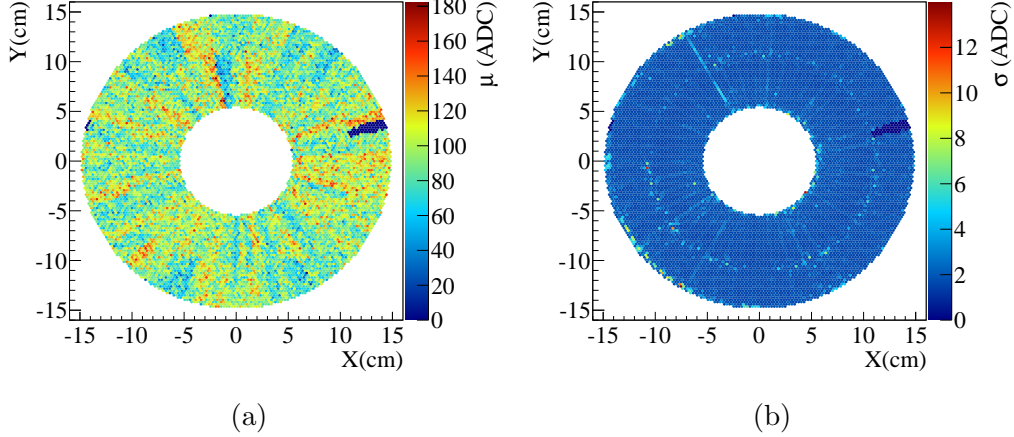


Figure 46: (a) Pedestals and (b) noise values in units of ADC channels as a function of the pad position. The dark blue areas correspond to defect electronic channels.

level, which can be seen in Fig. 46(b) is caused by channels on the edges of the block with longer track lengths from the connector to the chip on the front-end PCB.

### 12.3. Calibration of the gas gain

The gas gain is one of the key parameters which decisively influences the performance of the TPC in terms of spatial and energy resolution. For GEM detectors, the effective gain of the GEM stack is the important quantity, because it takes into account charge losses in the GEM structures. Using an X-ray source with known rate, it may be determined e.g. from the current measured on the readout pads. In addition to the absolute value of the effective gain, which determines the signal-to-noise ratio, local relative variations of it strongly impact the energy resolution of the detector and thus the  $dE/dx$  resolution. In multi-GEM detectors, such variations may arise from non-uniformities of the hole diameters or the foil spacings across the active area, and have been observed to be as large as 20 % [42]. Contributions to local variations of the gain can also originate from slightly varying electronic



conversion gains for individual channels of the front-end chips. In order not to compromise the  $dE/dx$  resolution of the detector, a gain homogeneity of 1 % across the GEM surface has to be achieved by a proper calibration. An elegant method to monitor and equalize the total gain (effective gas gain and electronic conversion gain) for each pad during data taking is by introducing metastable radioactive  $^{83m}\text{Kr}$  into the drift volume. This technique does not require any physical invasion of the detector and allows full coverage of its active volume, and has already been applied in various large TPCs (e.g. ALEPH [43], DELPHI [44], HARP [45], ALICE [9], STAR [46]).

In order to introduce  $^{83m}\text{Kr}$  into the GEM-TPC, a dedicated  $^{83}\text{Rb}$  source with an activity of 2.5 MBq was produced at the HSKP<sup>2</sup> cyclotron [47].  $^{83}\text{Rb}$  decays with a half-life of 86.2 d via electron capture into  $^{83}\text{Kr}$ , mostly populating an isomeric, metastable state at 41.55 keV with a half-life of 1.83 h. This state decays into the ground state via a short-lived excited state at 9.4 keV. Both transitions occur predominantly via internal conversion, producing short-ranged electrons. The resulting shell excitation is removed by X-rays or Auger electrons. The decay spectrum observed in the TPC thus shows several peaks between 9.4 keV and 41.6 keV.

The container for the  $^{83}\text{Rb}$  source can be seen in Fig. 47. It is connected to the gas input line of the GEM-TPC such that, when the corresponding valves are opened, the gas flows past the inner steel tube holding the radioactive material, carrying the evaporated  $^{83m}\text{Kr}$  into the chamber volume. The container shielding consists of 13 cm lead that absorbs higher energetic decay photons. During normal operation of the TPC the Rb container is bypassed. Dedicated Kr calibration runs have been performed regularly during beam times using a random trigger. The electrons emitted in the decay process are stopped quickly in the gas and lead to large but spatially confined clusters which are reconstructed using the reconstruction techniques described at the beginning of this section. Figure 49a shows an example of typical clusters created by Kr decays.

The total cluster amplitude spectrum (in units of ADC channels) measured in Ar/CO<sub>2</sub> (90/10) is shown in Fig. 49b. It depends on the deposited energy  $E$ , the mean energy required to create an electron-ion pair in the gas  $W$ , the effective gain  $G_{\text{eff}}$  and the conversion gain  $A$  of the readout system, measured

---

<sup>2</sup>Helmholtz-Institut für Strahlen- und Kernphysik, Nussallee 14-16, D-53115 Bonn

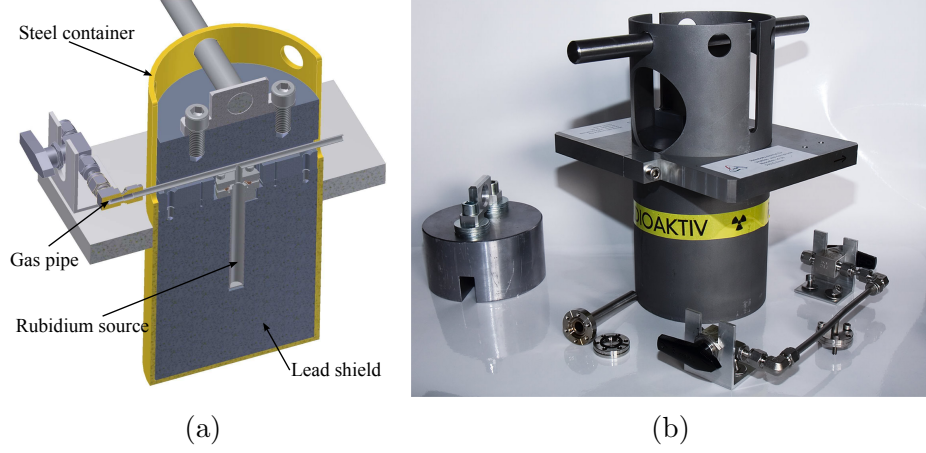


Figure 47: Lead-shielded container housing the  $^{83}\text{Rb}$  source. The source is contained in a steel finger that can be attached to the gas inlet via a bypass system. The outer shielding absorbs higher energetic decay photons that are emitted during the decay.

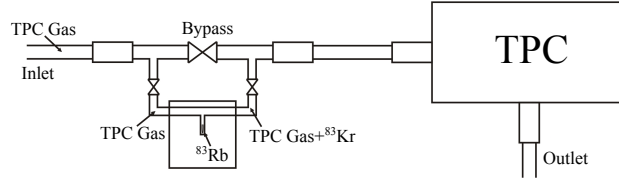


Figure 48: Sketch of the  $^{83}\text{Kr}$  container connected to the TPC gas system.

in  $e^-/\text{ADC}$  ch. (see section 7.5):

$$A_{\text{Kr}} = \frac{E}{W} \cdot \frac{G_{\text{eff}}}{A} \quad , \quad (1)$$

With  $W$  and  $A$  known, the absolute effective gain can be calibrated by reconstructing the full energy (41.5 keV) deposit of Kr decays. The resulting gain curve is displayed in Fig. 50 as a function of the scale factor applied to all GEM potentials (cf. Table 5 for the definition of the nominal setting corresponding to 100%). For Ar/CO<sub>2</sub> (90/10), a gain of approx. 2000 is achieved at a scale factor of 83%.

For a sufficiently large data sample this procedure also allows to extract pad-wise gain variations. To this end, the total charge of a reconstructed Kr cluster is assigned to the pad which contributed the pad hit with the

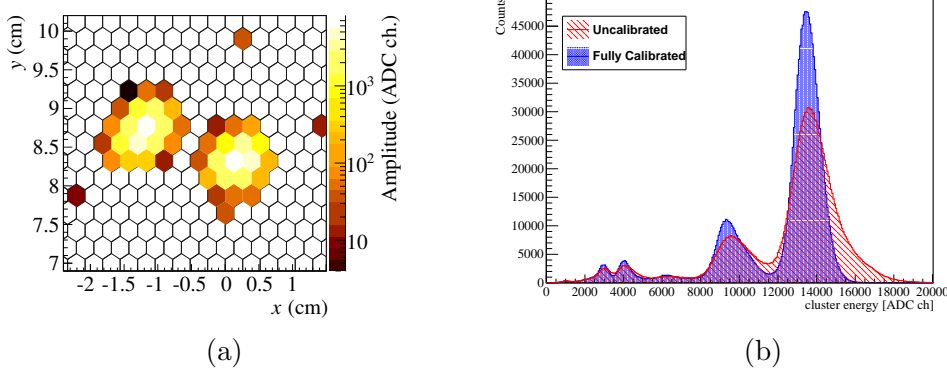


Figure 49: (a) Clusters from  $^{83m}\text{Kr}$  decays recorded in the GEM-TPC with a random trigger. (b) Cluster amplitude spectrum for Ar/CO<sub>2</sub> (90/10) recorded with the GEM-TPC at a voltage scaling factor of 81 %, (red) without and (blue) with pad-wise relative gain calibration.

largest amplitude, and an amplitude histogram is generated for every single pad. Only pads/channels with more than 500 entries are used for calibration. Pads with a distance to the outer or inner field-cage smaller than 5 mm are not taken into account as edge effects introduced by the field-cage walls deteriorate the measurement of the total charge. Finally, the gain equalization is performed by moving the median position of the main decay peak (41.5 keV) for all individual channels to the overall median position. From the relative shift a relative gain map is generated which is normalized to 1. The median was found to be less sensitive to outliers or values from failed fits than the mean. The relative calibration is done iteratively re-running the whole reconstruction and recursively correcting the gain factors.

Figure 51 shows the relative gain correction factors as a function of the pad positions obtained after 3 iterations. Pads with insufficient or no data (e.g. pads close to the field cage walls or broken electronic channels) are set to have correction factors of 1. Clearly visible are the sector boundaries of the last two GEM foils, slightly rotated with respect to each other, with a lower effective gain (i.e. correction factor  $> 1$ ). In addition, a darker, cross-shaped pattern is visible, most likely caused by stress applied during the glueing or mounting of the GEM stack. In these regions of larger foil tension, an increase in effective gain is observed (correction factors  $< 1$ ). Figure 51b shows a histogram of all gain calibration factors. The underlying distribution cen-

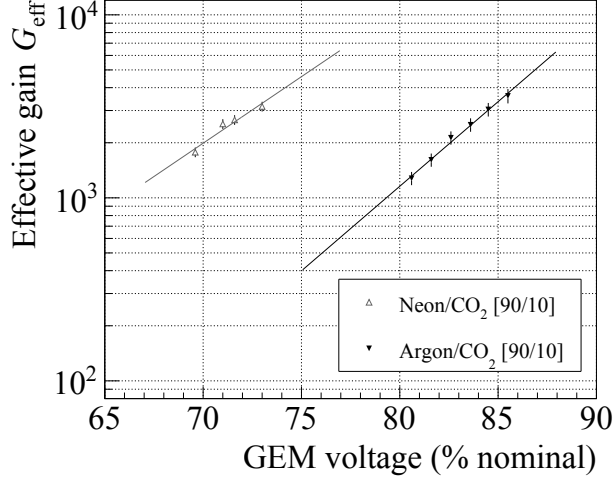


Figure 50: Effective gain  $G_{\text{eff}}$  of the GEM-TPC from Kr calibration runs as a function of the GEM voltage settings (cf. Table 5).

tered at 1 has an RMS of 0.086. The sharp peak at 1 comes from channels whose calibration factor was set to 1.

The Kr cluster amplitude spectrum measured with the GEM-TPC in Ar/CO<sub>2</sub> (90/10) gas at a voltage scaling factor of 81% is shown in Fig. 49b before (red) and after (blue) applying the pad-wise relative gain calibration. A clear separation of the main peaks can be observed while the double-peak-structure at 29/32.2 keV can not be clearly separated. An energy resolution of 7.2 % before and 4.1 % after calibration in the main 41.5 keV peak is achieved, i.e. the pad-wise calibration enhances the energy resolution of the detector at 41.5 keV by more than 40%. This translates into an improvement of 14.3% on the specific-energy resolution of the GEM-TPC [38, 39].

An important quantity which influences both the position and the energy resolution of the detector is the signal-to-noise ratio (SNR). It is defined as the maximum pad signal amplitude in a cluster divided by the corresponding pad noise value. Typically, the SNR is required be larger than 20 – 25 for TPCs [48]. The signal-to-noise ratio for the GEM-TPC for different values of the gas gain in Ar/CO<sub>2</sub> (90/10) is shown in Fig. 52.

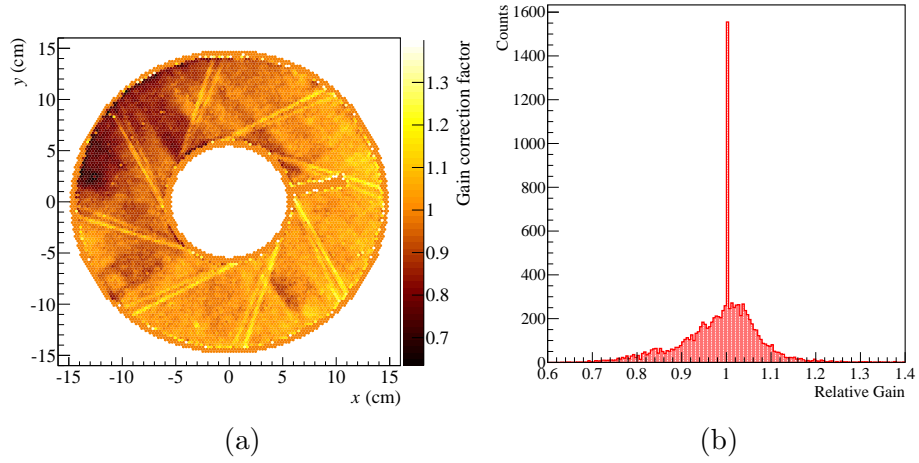


Figure 51: Figure (a) shows the relative gain calibration factors for all pads of the GEM-TPC as function of their position. Figure (b) shows the distribution of the calibration factors, which is centered at 1 has an RMS of 0.09. The peak at 1 arises from channels for which no calibration was possible and which were consequently set to 1.

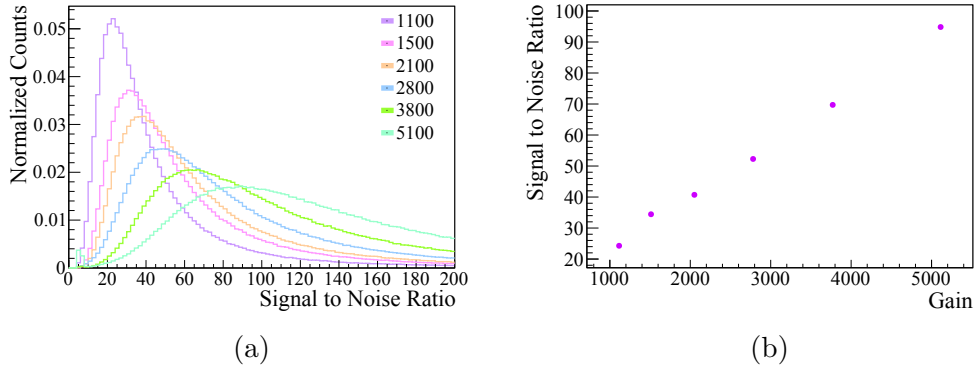


Figure 52: Signal to noise ratio calculated by dividing the highest pad amplitude in a cluster by the noise of the corresponding pad. The left plot shows the distributions for various gain settings in Ar/CO<sub>2</sub> (90/10) while the right panel shows the position of the most probable value of these distributions as a function of the gain. Note that the error bars are smaller than the points.

selection criteria	Value
cluster size	$> 2$ pad hit
cluster amplitude	$> 50$ ADC channels
radial position (min.)	$> 57$ mm
radial position (max.)	$< 148$ mm

Table 6: Cuts applied to select clusters for the measurement of the drift velocity.

#### 12.4. Determination of the drift velocity

The resolution of a TPC relies critically on the knowledge of the drift velocity of electrons. The drift velocity depends on many parameters such as the exact gas mixture, potential impurities like water and oxygen, the temperature and pressure of the gas, and the exact values of the electric and magnetic fields. Since not all of these parameters might be known with the required accuracy, it is important to be able to determine the drift velocity in situ from the data.

If the maximum drift time of electrons in the TPC is smaller than the read-out time window given by the product of the maximal number of samples (511) and the time length per sample (64.3 ns for a sampling frequency of 15.55 MHz), the full drift window of the TPC is read out. The average drift velocity can then be determined using the drop of the cluster occupancy at the geometric boundaries imposed by the cathode and the GEM foil closest to the drift volume. The measured cluster occupancy distribution as a function of the time obtained from cosmic muon data at a drift field of  $309.6 \text{ V cm}^{-1}$  is shown in Fig. 53. The clusters used for this procedure are constructed as described in 12.1. Table 6 shows the cuts applied to select good clusters and to reduce background contributions. Error functions are fitted to the occupancy distribution in order to determine the position of the cathode and the first GEM foil. The inflection points of these functions are used to determine the edges of the drift volume. With the difference between the two edges in units of ADC samples,  $N_{\text{cathode}} - N_{\text{GEM1}}$ , the sampling rate  $SR$  of the front-end chip and the known distance  $l$  between the chamber edges, the drift velocity averaged over the full volume can be calculated by

$$v_{\text{drift}} = \frac{l \cdot SR}{N_{\text{cathode}} - N_{\text{GEM1}}}. \quad (2)$$

The same method can also be used for measurements with particle beams,

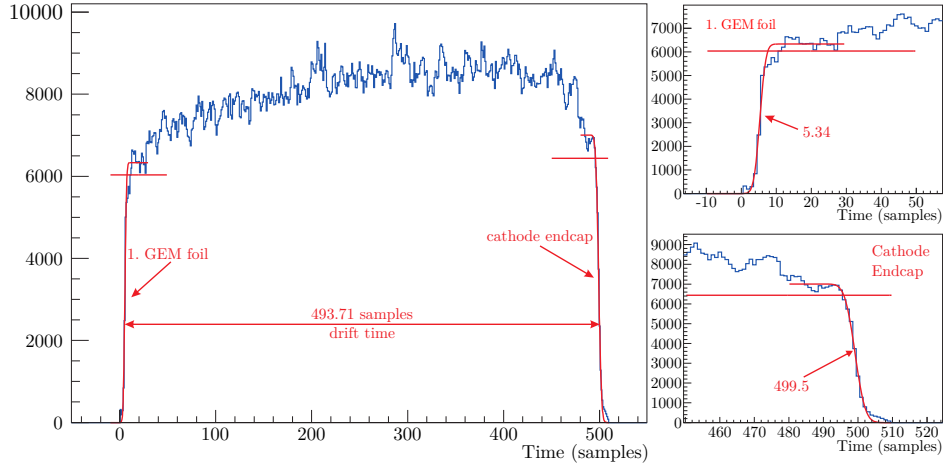


Figure 53: Time spectrum of clusters from cosmics with fitted error functions. For the measurement shown, the drift field was set to  $309.6 \text{ V cm}^{-1}$  in  $\text{Ar}/\text{CO}_2$  (90/10).

provided the drift velocity is large enough so that the full drift length is visible. In Fig. 54 one can see a cluster time spectrum obtained with a  $1.7 \text{ GeV}/c \pi^-$  beam at a drift field of  $302.4 \text{ V cm}^{-1}$  in  $\text{Ar}/\text{CO}_2$  (90/10) gas. Two targets were installed in the central bore of the TPC, a Pb and a Cu disk 180 mm further downstream, which are visible as pronounced drops in the occupancy in Fig. 54. In case the physical boundaries of the drift volume are not visible, e.g. because of a smaller drift field, the known target positions may be used to perform the drift velocity calibration instead [37].

Figure 55 shows the time evolution of drift velocities determined by fitting the end-cap positions for different data taking periods (left: pion beam, right: cosmics), compared to drift velocities calculated with Magboltz [49]. These take into account the gas temperatures and pressures measured at the inlet to the TPC located in the media flange. The uncertainties shown for the Magboltz calculation take into account the variations of the pressure and temperature measurements around their average values. The uncertainties for the measured values are the statistical uncertainties of the error function fits.

One can see that the relative differences between measurement and Magboltz calculations are below 4% for the pion beam measurement and in between 2% and 6% for the cosmic muon measurement. The systematic shift between measured and calculated drift velocity is attributed to a possible bias in the

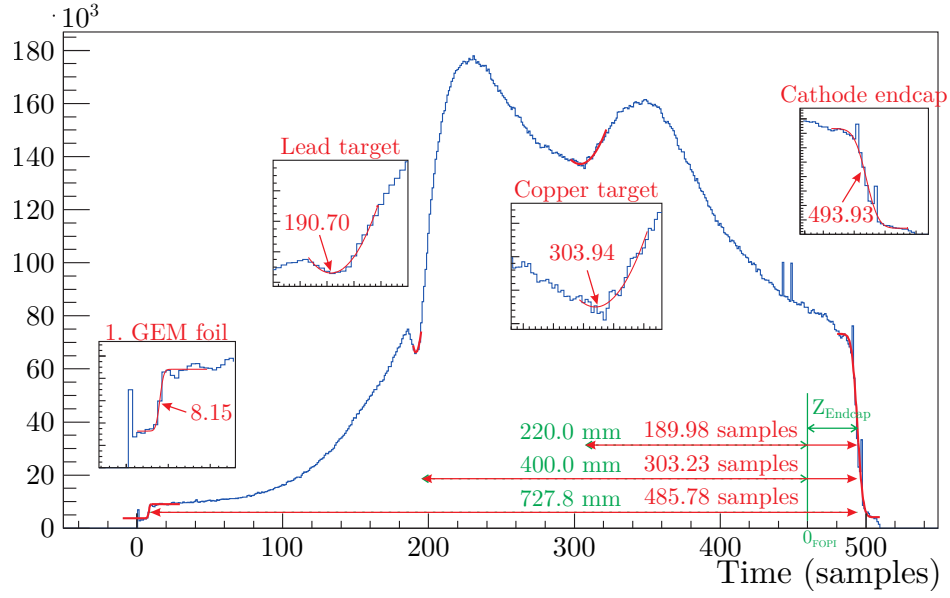


Figure 54: Time spectrum of clusters from a measurement with beam pions hitting a Pb and a Cu target inserted into the inner bore of the TPC. The spectrum has been taken during the  $\pi^-$  beam time 2011 at the FOPI experiment in Ar/CO<sub>2</sub> (90/10) gas with a drift field of  $E_{\text{drift}} = 302.4 \text{ V cm}^{-1}$ .

temperature and pressure measurements, which may not reflect the actual gas conditions and to a systematic uncertainty of the actual drift length. For the future, it is planned to extract the drift velocity from the alignment procedure using particle tracks which are measured both in the GEM-TPC and the CDC of the FOPI experiment. In addition, a more precise measurement of the actual gas pressure and temperature is envisaged.

### 13. Conclusions

A large TPC with GEM amplification and without gating grid was built and successfully tested to demonstrate its applicability in future high-rate experiments such as ALICE at CERN. The detector features a number of innovative elements such as an extremely light-weight and gas-tight vessel, which serves as field cage and gas container at the same time, a stack of large disk-shaped sectorized GEM foils integrated in a media flange which forms the detector end cap, or a readout plane with 10,254 hexagonal pads in order



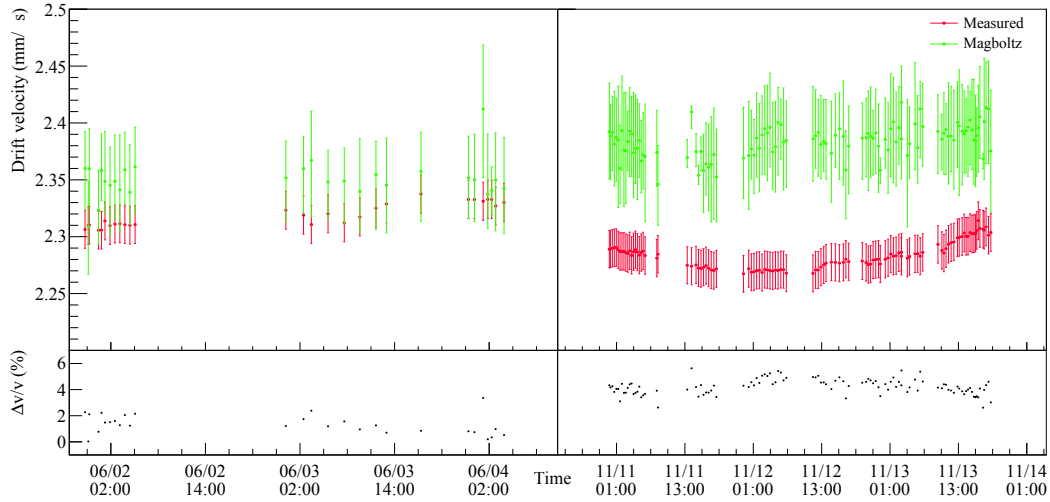


Figure 55: Comparison of (red) measured and (green) calculated drift velocities as a function of time during the (left) pion beam and (right) cosmic muon measurement campaigns. The calculation with Magboltz takes into account the measured values of temperature, pressure, drift field and their respective variations during one measurement. The uncertainties for the calculated drift velocities are mainly governed by the rather big variations of the temperature and pressure measurements. The lower part of the image shows the relative difference between the drift velocity calculated by Magboltz and the measured drift velocity.

to minimize the pad angular effect. The signals induced on the pad-plane are read out using AFTER/T2K ASICs mounted on fully custom-made front-end cards and ADCs.

First commissioning results of the system have been shown, which prove the feasibility of this novel detector type. The chamber itself as well as all custom-made supporting infrastructure such as the cooling circuit, the gas supply, and the slow-control system have shown excellent performance during data taking with cosmic rays and various particle beams as part of the FOPI spectrometer. Calibration procedures have been established and put into operation, such as pedestal and noise determination, gain calibration and equalization based on the injection of metastable  $^{83}\text{Kr}$  into the detector gas, and drift velocity determination.

These results raise the expectation that (i) the GEM-TPC will significantly improve the performance of the FOPI experiment by enhancing the vertex resolution, the secondary vertex reconstruction and the global event recon-

struction, and that (ii) an ungated TPC with GEM amplification will allow us to overcome the large deadtime associated with classical TPCs, and thus open many new areas of application of this powerful detector type.

## **Acknowledgements**

We express our gratitude to the engineers and technicians from GSI Darmstadt, TU München, Universität Bonn, and SMI Vienna, who have contributed to the construction and commissioning of the GEM-TPC.

We acknowledge support from Bundesministerium für Bildung und Forschung, (Grant agreement no. 06MT245I, 06MT9165I, 05P12WOCAA, 05P12WOGHH), DFG cluster of excellence “Origin and Structure of the Universe”, DFG SFB/TR16 “Elektromagnetische Anregung subnuklearer Systeme”, GSI Forschungs- und Entwicklungsauftrag (Grant agreement no. TMPAUL, TMPAUL1012, TMFABI1012, TMLFRG1316F), Helmholtz Association (Young Investigator Group VH-NG-330), European Union FP7 (HadronPhysics2, Grant agreement no. 227431; HadronPhysics3, Grant agreement no. 283286).

## References

- [1] D. R. Nygren, J. N. Marx, The Time Projection Chamber, *Phys. Today* 31N10 (1978) 46–53.
- [2] R. J. Madaras, et al., Spatial resolution of the PEP-4 Time Projection Chamber, *IEEE Trans. Nucl. Sci.* 30 (1983) 76–81.
- [3] W. B. Atwood, et al., Performance of the ALEPH time projection chamber, *Nucl. Instr. Meth. A* 306 (1991) 446–458. doi:10.1016/0168-9002(91)90038-R.
- [4] C. Brand, et al., The DELPHI Time Projection Chamber, *Nucl. Instr. Meth. A* 283 (1989) 567–572. doi:10.1109/23.34417.
- [5] S. Wenig, Performance of the large-scale TPC system in the CERN heavy ion experiment NA49, *Nucl. Instr. Meth. A* 409 (1998) 100–104. doi:10.1016/S0168-9002(97)01245-X.
- [6] S. Afanasev, et al., The NA49 large acceptance hadron detector, *Nucl. Instr. Meth. A* 430 (1999) 210–244. doi:10.1016/S0168-9002(99)00239-9.
- [7] K. H. Ackermann, et al., The STAR time projection chamber, *Nucl. Phys. A* 661 (1999) 681–685. doi:10.1016/S0375-9474(99)85117-3.
- [8] K. H. Ackermann, et al., The forward time projection chamber (FTPC) in STAR, *Nucl. Instr. Meth. A* 499 (2003) 713–719. arXiv:nucl-ex/0211014, doi:10.1016/S0168-9002(02)01968-X.
- [9] J. Alme, et al., The ALICE TPC, a large 3-dimensional tracking device with fast readout for ultra-high multiplicity events, *Nucl. Instr. Meth. A* 622 (2010) 316–367. arXiv:1001.1950, doi:10.1016/j.nima.2010.04.042.
- [10] G. Charpak, R. Bouclier, T. Bressani, J. Favier, C. Zupancic, The use of multiwire proportional counters to select and localize charged particles, *Nucl. Instr. Meth.* 62 (1968) 262–268.
- [11] F. Sauli, GEM: A new concept for electron amplification in gas detectors, *Nucl. Instr. Meth. A* 386 (1997) 531–534.

- [12] F. Sauli, S. Kappler, L. Ropelewski, Electron collection and ion feedback in GEM-based detectors, in: Nuclear Science Symposium Conference Record, 2002. NSS '02. IEEE, IEEE, Piscataway, NJ, 2002.
- [13] C. Altunbas, M. Capeáns, K. Dehmelt, J. Ehlers, J. Friedrich, I. Konorov, A. Gandi, S. Kappler, B. Ketzer, R. D. Oliveira, S. Paul, A. Placci, L. Ropelewski, F. Sauli, F. Simon, M. van Stenis, Construction, test and commissioning of the triple-GEM tracking detectors for COMPASS, Nucl. Instr. Meth. A 490 (2002) 177–203.
- [14] B. Ketzer, Q. Weitzel, S. Paul, F. Sauli, L. Ropelewski, Performance of triple GEM tracking detectors in the COMPASS experiment, Nucl. Instr. Meth. A 535 (1) (2004) 314–318. doi:10.1016/j.nima.2011.06.028.  
URL <http://www.sciencedirect.com/science/article/pii/S0168900211011442>
- [15] P. Abbon, et al., The COMPASS experiment at CERN, Nucl. Instr. Meth. A 577 (2007) 455–518. arXiv:hep-ex/0703049.
- [16] B. Ketzer, A. Austregesilo, F. Haas, I. Konorov, M. Krämer, A. Mann, T. Nagel, S. Paul, A triple-gem detector with pixel readout for high-rate beam tracking in compass, in: Nuclear Science Symposium Conference Record, 2007. NSS '07. IEEE, Vol. 1, IEEE, Piscataway, NJ, 2007, pp. 242–244. doi:10.1109/NSSMIC.2007.4436323.
- [17] G. Bencivenni, et al., A triple GEM detector with pad readout for high rate charged particle triggering, Nucl. Instr. Meth. A 488 (2002) 493–502. doi:10.1016/S0168-9002(02)00515-6.
- [18] Z. Fraenkel, et al., A hadron blind detector for the PHENIX experiment at RHIC, Nucl. Instr. Meth. A 546 (2005) 466–480. arXiv:physics/0502008, doi:10.1016/j.nima.2005.02.039.
- [19] M. G. Bagliesi, et al., The TOTEM T2 telescope based on triple-GEM chambers, Nucl. Instr. Meth. A 617 (2010) 134–137. doi:10.1016/j.nima.2009.07.006.
- [20] G. Bencivenni, D. Domenici, An ultra-light cylindrical GEM detector as inner tracker at KLOE-2, Nucl. Instr. Meth. A 581 (2007) 221–224. doi:10.1016/j.nima.2007.07.082.

- [21] D. Abbaneo, et al., Characterization of GEM Detectors for Application in the CMS Muon Detection System [arXiv:1012.3675](#).
- [22] M. Ball, K. Eckstein, T. Gunji, Ion backflow studies for the ALICE TPC upgrade with GEMs, JINST 9 (2014) C04025. doi:[10.1088/1748-0221/9/04/C04025](#).
- [23] ALICE collaboration, Addendum to the Technical Design Report for the Upgrade of the ALICE Time Projection Chamber, Tech. Rep. CERN-LHCC-2015-002. ALICE-TDR-016-ADD-1, CERN, Geneva (Feb 2015). URL <https://cds.cern.ch/record/1984329>
- [24] B. Ketzer, A Time Projection Chamber for High-Rate Experiments: Towards an Upgrade of the ALICE TPC, Nucl. Instr. Meth. A 732 (2013) 237–240. [arXiv:1303.6694](#), doi:[10.1016/j.nima.2013.08.027](#).
- [25] ALICE collaboration, Upgrade of the ALICE Time Projection Chamber, Tech. Rep. CERN-LHCC-2013-020. ALICE-TDR-016, CERN, Geneva (Oct 2013). URL <https://cds.cern.ch/record/1622286>
- [26] M. Lang, Upgrade for the CBELSA/TAPS experiment at ELSA for eta and eta-prime decays, Int. J. Mod. Phys. E19 (2010) 938–945. doi:[10.1142/S0218301310015382](#).
- [27] K. Hildenbrand, One year of operating FOPI: Results and status of the  $4\pi$  detector facility at SIS/ESR, GSI Nachr. 91-02 (1992) 6–16.
- [28] R. Brun, F. Rademakers, ROOT - An object oriented data analysis framework, Nuclear Instruments and Methods in Physics Research Section A: Accelerators, Spectrometers, Detectors and Associated Equipment 389 (12) (1997) 81 – 86, new Computing Techniques in Physics Research V. doi:[http://dx.doi.org/10.1016/S0168-9002\(97\)00048-X](http://dx.doi.org/10.1016/S0168-9002(97)00048-X).
- [29] S. Bachmann, A. Bressan, M. Capeáns, M. Deutel, S. Kappler, B. Ketzer, A. Polouektov, L. Ropelewski, F. Sauli, E. Schulte, L. Shekhtman, A. Sokolov, Discharge studies and prevention in the gas electron multiplier (GEM), Nucl. Instr. Meth. A 479 (2002) 294–308, CERN-EP-2000-151.

- [30] M. Berger, Development, Commissioning and Spatial Resolution Studies of a new GEM based TPC, Ph.D. thesis, Technische Universität München (2015).
- [31] S. Barboza, M. Bregant, et al., SAMPA chip: a new ASIC for the ALICE TPC and MCH upgrades, Journal of Instrumentation 11 (02) (2016) C02088.  
URL <http://stacks.iop.org/1748-0221/11/i=02/a=C02088>
- [32] C. Hearty, et al., T2K ND 280 TPC technical design report version 1.0T2K Internal Note.
- [33] P. Baron, et al., AFTER, an ASIC for the readout of the large T2K time projection chambers, IEEE Trans. Nucl. Sci. 55 (2008) 1744–1752. doi:10.1109/TNS.2008.924067.
- [34] G. Baum, et al., COMPASS: A proposal for a COmmon Muon and Proton Apparatus for Structure and Spectroscopy, CERN/SPSLC 96-14, SPSC/P 297 (March 1996).
- [35] Huber Kältemaschinenbau GmbH, UCH080T-H, [www.huber-online.com](http://www.huber-online.com).
- [36] Phillip Müllner, A GEM based Time Projection Chamber prototype for the PANDA experiment - Gas system development and forward tracking studies, Ph.D. thesis, Universität Wien (2012).
- [37] D. Kaiser, Steuerung und Überwachung einer Zeitprojektionskammer mit GEM-Auslese, Ph.D. thesis, Rheinische Friedrich-Wilhelms-Universität Bonn (2014).  
URL <http://hss.ulb.uni-bonn.de/2014/3530/3530.htm>
- [38] F. Böhmer, M. Ball, S. Dørheim, K. Eckstein, A. Hönle, C. Höppner, B. Ketzer, et al., First measurement of  $dE/dx$  with a GEM-based TPC, Nucl. Instr. Meth. A 737 (2014) 214–221. doi:10.1016/j.nima.2013.10.094.
- [39] F. Böhmer, Development of a GEM-based TPC for the measurement of in-medium signatures in kaon momenta in a combined setup at fopi, Ph.D. thesis, Techn. Univ. München (2015).

- [40] M. Ball, F. Böhmer, S. Dørheim, C. Höppner, B. Ketzer, et al., Technical Design Study for the PANDA Time Projection Chamber [arXiv:1207.0013](#).
- [41] F. Sauli, Principles of operation of multiwire proportional and drift chambers, CERN, CERN, Geneva, 1977, p. 92 p, CERN, Geneva, 1975 - 1976.
- [42] L. Hallermann, Analysis of GEM properties and development of a GEM support structure for the ILD Time Projection Chamber, Ph.D. thesis, DESY (2010).
- [43] D. Decamp, B. Deschizeaux, et al., ALEPH: A detector for electron-positron annihilations at LEP, NIMA 294 (1-2) (1990) 121 – 178. doi:[DOI:10.1016/0168-9002\(90\)91831-U](#).
- [44] A. De Min, et al., Performance of the HPC calorimeter in DELPHI, IEEE Trans. Nucl. Sci. 42 (1995) 491–498. doi:[10.1109/23.467923](#).
- [45] F. Dydak, A. De Min, Analysis of harp tpc krypton data, HARP memo 04-103, submitted 28 April 2004 corrected 7 May 2004 updated 10 June 2004.
- [46] T. Eggert, Calibration of the STAR Forward Time Projection Chamber with Krypton-83m, Star Note 424.
- [47] M. Rasulbaev, K. Maier, R. Vianden, T. Thmmler, B. Ostrick, C. Weinheimer, Production of 83rb for the katrin experiment, Applied Radiation and Isotopes 66 (12) (2008) 1838 – 1843. doi:[DOI:10.1016/j.apradiso.2008.04.020](#).
- [48] G. Dellacasa, et al., ALICE technical design report of the time projection chamber, Tech. rep., CERN (2000).
- [49] S. Biagi, Monte carlo simulation of electron drift and diffusion in counting gases under the influence of electric and magnetic fields, Nucl. Instr. Meth. A 421 (1 - 2) (1999) 234 – 240. doi:[http://dx.doi.org/10.1016/S0168-9002\(98\)01233-9](#).